Journal of Materials Chemistry A

ROYAL SOCIETY OF CHEMISTRY

REVIEW

View Article Online
View Journal

Cite this: DOI: 10.1039/d5ta07726e

Sodium-ion battery development since 2020 with future perspectives†

Abu Faizal Abdul Salam, [a] Xiaoran Zheng, [b] Zhao Chen,[a] Yi Liao,[a] Do Kyung Kim, [cd] Sajjad Seifi Mofarah, [b] Pramod Koshy, [b] Neeraj Sharma *[a] and Dong Jun Kim *[a]

Sodium-ion batteries are emerging as low-cost, sustainable alternatives to lithium-ion systems, particularly for applications where energy density can be traded for safety, raw material abundance, and manufacturing simplicity. This review examines recent advances in electrode design, with emphasis on how structural modifications at the atomic and mesoscale influence electrochemical performance. In cathodes, developments in layered oxides such as P2, O3, and their biphasic hybrids have demonstrated how compositional tuning and interface engineering can suppress phase transitions and activate oxygen redox. Polyanionic compounds and Prussian blue analogues provide distinct pathways for achieving structural stability and high-rate performance, supported by inductive effects and open-framework geometries. High entropy strategies have emerged as a unifying design principle that enables simultaneous optimisation of redox activity, sodium-ion diffusion, and phase robustness across multiple material classes. On the anode side, the performance of hard carbon has been advanced through control of pore architecture, heteroatom doping, and interfacial engineering to improve initial coulombic efficiency. Finally, we highlight trends in industrial translation, including full-cell architectures, standardisation protocols, and scalable synthesis. Overall, these developments outline a maturing field defined by increasingly sophisticated materials chemistry and growing commercial viability.

Received 20th September 2025
Accepted 26th December 2025

DOI: 10.1039/d5ta07726e

rsc.li/materials-a

1. Introduction

Within the world's current energy storage landscape, sodium-ion batteries (SIBs) stand out as a promising candidate for next-generation energy storage. Natural abundance of sodium and broad distribution could help ease supply chain constraints and reduce raw material costs.[1] Furthermore, the electrochemical similarities between sodium and lithium allow researchers to build upon decades of lithium-ion battery (LIB) development to advance SIB technologies. The growing momentum toward electrification and cost-effective energy storage is reflected in the steadily increasing number of publications in this field each year (Fig. 1). Yet SIBs face challenges that set them apart from lithium-based configurations.

A central obstacle is the larger ionic radius of sodium ions compared to lithium ions, which hampers intercalation kinetics and imposes mechanical stress on host materials during cycling. This size difference has significant implications for ion mobility within host crystal structures and necessitates

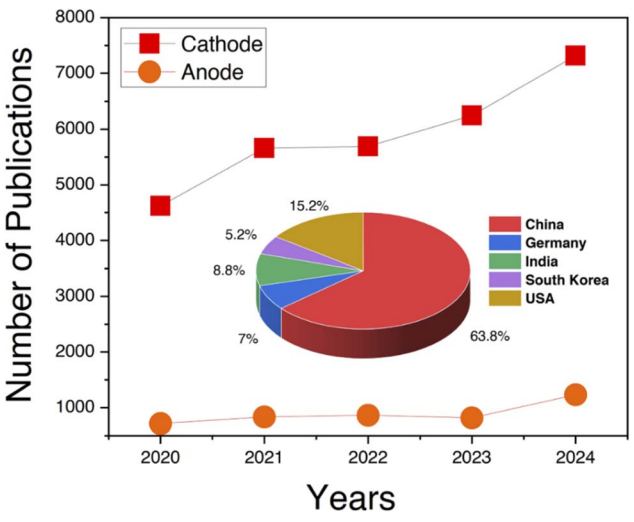

Fig. 1 Number of publications in the field of SIBs between the years 2020–2024. Data collated from Web of Science.

[a]School of Chemistry, The University of New South Wales, Sydney, NSW 2052, Australia

[b]School of Material Science and Engineering, The University of New South Wales, NSW 2052, Australia

[c]School of Mechanical and Manufacturing Engineering, The University of New South Wales, NSW 2052, Australia

[d]Department of Materials Science and Engineering, Korea Advanced Institute of Science and Technology (KAIST), Daejeon 34141, Republic of Korea. E-mail: dongjun.kim@unsw.edu.au; neeraj.sharma@unsw.edu.au

† Dedication: this article is dedicated to Shatiswar Prasad Sharma, a loving and supporting father.

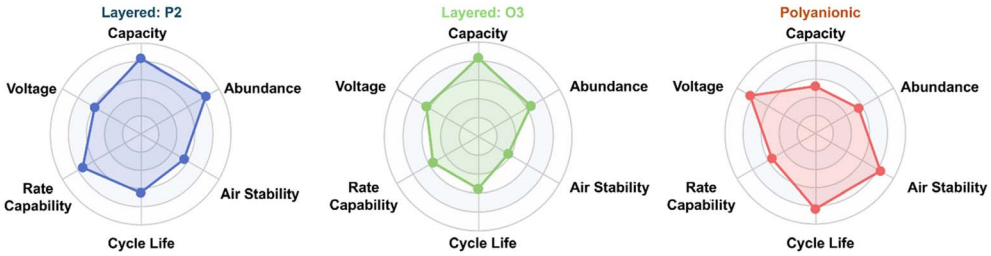

Fig. 2 Comparison of performance metrics for layered P2, O3 and polyanionic sodium-ion cathodes.

electrode materials capable of accommodating larger sodium ions without inducing excessive lattice strain or irreversible phase transitions. The larger radius often results in lower diffusion coefficients, which can limit the rate performance of SIBs compared to lithium-based systems.[2]

In addition, the standard redox potential of the Na^+/Na couple (−2.71 V *vs.* SHE) is slightly higher than that of Li^+/Li (−3.04 V *vs.* SHE).[3] This difference results in lower overall cell voltages for SIBs when analogous cathode chemistries are employed. Consequently, SIBs typically exhibit reduced energy densities relative to LIBs. However, careful selection of electrode materials and cell architectures has been shown to mitigate these limitations to a considerable extent.

Another critical aspect of SIB development is the formation of the solid electrolyte interphase (SEI), which is essential for long-term cycling stability and high coulombic efficiency. While extensive insights exist regarding SEI formation and composition in lithium systems, the understanding of these processes in sodium-based systems remains less developed. The differing solvation structures and desolvation energies of sodium-ions, combined with its larger size, often result in unique SEI characteristics that influence both electrochemical stability and interfacial kinetics.[4]

Moreover, the choice of electrolyte systems for SIBs must strike a balance between redox stability and chemical compatibility with sodium-based electrodes. Many non-aqueous solvents used in LIBs can be adapted for sodium systems, however, variations in solvent-ion interactions, viscosity, and ionic conductivity necessitate tailored formulations.[5] Aqueous SIBs, while attractive for safety and cost reasons, are constrained by the narrow electrochemical stability window of water. This necessitates electrode materials that operate within a reduced voltage range to avoid parasitic reactions such as hydrogen or oxygen evolution.

Despite these obstacles, notable progress has been made in recent years. Advances in material composition, nanoscale engineering, and interface design have improved capacity retention, rate capability, and thermal stability.[6–8] Furthermore, strategies such as high entropy materials, defect modulation, and advanced surface coatings are expanding the performance limits of SIB electrodes.[9]

Nevertheless, recent studies indicate that SIBs are unlikely to replace LIBs in the immediate future, particularly in high-performance applications such as electric vehicles. Instead, SIBs are increasingly viewed as a complementary technology, well-suited for scenarios where moderate energy density is sufficient, such as grid-scale storage.[10] Their future competitiveness will depend on further improvements in energy density, refinements in manufacturing processes, and continued innovation in electrode materials. Importantly, sodium-ion systems offer strategic value as a safeguard against fluctuations in the supply chains of critical minerals, underlining their potential role within a diversified energy storage portfolio.

In this review, we examine recent progress in the development of electrode materials for SIBs, with particular focus on structures, electrochemical behaviour, and performance metrics reported since 2020. Fig. 2 presents a radar plot illustrating the comparative performance of various sodium cathode types. In this work, we discuss key material classes and their relationship to performance (Table 1), identify ongoing challenges, and consider how recent innovations are shaping the outlook for SIBs as practical and sustainable solutions for applications ranging from grid integration to cost-sensitive electric mobility.

2. Positive electrode materials

2.1. Layered oxides

Layered oxide cathodes have emerged as a central focus in the development of SIBs, offering an appealing combination of high theoretical capacities, tunable redox potentials, and relatively mature synthesis routes. Despite these advantages, the practical deployment of these systems remains constrained by challenges such as structural instabilities, complex phase transitions, and pronounced sensitivity to atmospheric moisture.[44]

Among the layered materials, P2-type oxides are characterised by sodium ions occupying prismatic sites between layers of edge-sharing MO_6 octahedra (Fig. 2a).[45] This arrangement creates wider channels that facilitate relatively rapid sodium diffusion, contributing to relatively good rate capabilities.[45] Nonetheless, P2 phases are susceptible to structural changes at high states of charge, including sodium-vacancy ordering and phase transitions, which can compromise long-term stability and capacity retention.

In contrast, O3-type layered oxides feature sodium ions located in octahedral sites between transition-metal (TM) oxide layers arranged in an ABCABC stacking sequence (Fig. 2a).[45] These structures accommodate higher sodium content, resulting in greater theoretical capacities. However, O3-type materials

Table 1 Literature of selected cathode materials used in SIBs, their electrochemical performance and the relevant section they are presented in this work

Sections	Chemical formula	Practical capacity [theoretical capacity] (mAh g^{-1})	Average voltage (V *vs.* Na^+/Na)	Ref.
1.1.1	$Na_{2/3}[Mn_{2/3}Ni_{1/3}]O_2$	167 [172.61]	1.5–4	11
	$Na_{0.612}$ $K_{0.056}$ MnO_2	240.5 [158.95]	1.8–4.3	12
	$Na_{0\cdot85}Li_{0\cdot12}Ni_{0\cdot22}Mn_{0\cdot66}O_2$	110 [224.3]	2–4.6	13
	P2–$Na_{2/3}Ni_{0.3}Mn_{0.7}O$	89.4 [172.8]	2–4	14
	$Na_{2/3}Li_{0.05}Ni_{1/3}Mn_{2/3}O_2$	86.4 [172.03]	2–4	15
	$Na_{0.67}MnO_2$	176 [175.45]	2.0–4.4	16
	$K_{0.4}[Ni_{0.2}Mn_{0.8}]O_2$	194	1.5–4.2	17
	$Na_{0.75}Mg_{0.25}Mn_{0.75}O_2$	166 [208.257]	1.5–4	18
	$Na_{0.7}Li_{0.03}[Mg_{0.15}Li_{0.07}Mn_{0.75}]O_2$	266 [200.36]	1.5–4.6	19
1.1.2	$Na_{0.9}Ca_{0.05}Ni_{1/3}Fe_{1/3}Mn_{1/3}O_2$	116.3 [216.9]	2–4	20
	$Na_{0.93}Li_{0.12}Ni_{0.25}Fe_{0.15}Mn_{0.48}O_2$	130.1 [240.52]	2–4.2	21
	$NaMn_1/_3Fe_1/_3Ni_1/_3O_2$	160 [240.6]	1.5–4.6	22
	Sn doped $NaNi_{1/3}Fe_{1/3}Mn_{1/3}O_2$	126.9 [240.6]	2.0–4.1	23
	$Na_{0.9}Ni_{0.32}Zn_{0.08}Fe_{0.1}Mn_{0.3}Ti_{0.2}O_2$	144.9 [222.5]	2–4	24
	$Na_{0.8}Li_{0.2}Fe_{0.2}Ru_{0.6}O_2$	148 [173.4]	1.5–4.5	25
	$Na(Fe_{0.2}Co_{0.15}Cu_{0.05}Ni_{0.2}Mn_{0.2}Ti_{0.2})B_{0.02}O_2$	121 [242.1]	2–4.1	26
	$NaNi_{0.32}Fe_{0.32}Mn_{0.32}Al_{0.02}Cu_{0.02}O_2$	140 [243.6]	2–4	27
	$Na_{0.85}Mn_{0.45}Ni_{0.25}Li_{0.05}Cu_{0.1}Ti_{0.15}O_2$	134.9 [217]	2–4.2	28
	$Na_{0.7}Mn_{0.4}Ni_{0.3}Cu_{0.1}Fe_{0.1}Ti_{0.1}O_{1.95}F_{0.1}$	126.4 [177.8]	1.5–4.2	29
	$Na_{0.67}Ni_{0.19}Li_{0.08}Mg_{0.06}Mn_{0.67}O_2$	90.3 [184]	2.5–4.3	30
	$Na_{0.72}Mn_{0.4}Fe_{0.4}Ti_{0.1}$ $Cu_{0.1}O_2$	114 [187.3]	2.3–4.2	31
1.1.3	$Na_{0.8}Mg_{0.06}Ni_{0.34}Mn_{0.54}Ti_{0.06}O_2$	154.5 [205.5]	2.2–4.4	32
	$Na_{0.8}Ni_{0.23}Fe_{0.34}Mn_{0.43}O_2$	146.4 [201.5]	2–4	33
	$NaNi_{0\cdot12}Cu_{0\cdot12}Mg_{0\cdot12}Fe_{0\cdot15}Co_{0\cdot15}Mn_{0\cdot1}Ti_{0\cdot1}Sn_{0\cdot1}Sb_{0\cdot04}O_2$	110 [229.4]	2–3.9	34
1.3.1	$NaCu_{0\cdot1}Ni_{0\cdot2}Co_{0\cdot2}Fe_{0\cdot2}Mn_{0\cdot15}Ti_{0\cdot15}O_2$	123.3 [240.8]	2–4.1	35
	$Na_{3.4}Fe_{0.4}Mn_{0.4}V_{0.4}Cr_{0.4}Ti_{0.4}(PO_4)_3$	161.3 [194.9]	1.5–4.5	36
1.3.2	$Na_3VAl_{0.2}Cr_{0.2}Fe_{0.2}In_{0.2}Ga_{0.2}(PO_4)_3$	102 [171.5]	2.5–4.4	37
	$Na_{2.48}(Fe_{0.89}$ $Mg_{0.03}$ $Sn_{0.04})_{1.76}$ $(SO_4)_3$	83 [150.3]	2–4.5	38
	$Na_{2.72}Fe_{1.64}(SO_4)_3$	110.5 [164.7]	2–4.5	39
	$Na_3V_{2-x}Ce_{0.1}(PO_4)_2F_3$	111.5 [188.4]	2–4.5	40
	$Na_4Fe_{2.94}La_{0.04}(PO_4)_2(P_2O_7)$	128.4 [171.4]	1.7–4.3	41
	$Na_{3+4x}MnTi_{1-x}(PO_4)_3$	176 [197.6]	2–4	42
	$Na_7Fe_7(PO_4)_6F_3$	87 [159.2]	1.5–4.2	43

face challenges related to slower ionic mobility and significant sensitivity to air exposure. Sodium diffusion in these phases requires migration through narrower bottleneck pathways between adjacent octahedral sites, leading to higher energy barriers and more limited rate performance.

Recognising the complementary strengths and limitations of these two structures, recent research has focused on developing hybrid biphasic systems that combine both P2 and O3 phases. Such materials aim to harness the fast ion transport of P2 structures alongside the higher sodium content of O3 phases, offering a potential pathway to improved performance and stability.[45]

Beyond conventional TM redox mechanisms, oxygen redox has emerged as a promising avenue for enhancing capacity in layered oxide cathodes.[46] However, engaging oxygen often brings structural challenges that can undermine long-term performance.[46] While advances in material design and compositional control have shown potential to address these issues, significant hurdles remain. Realising practical SIB will depend on achieving stable cycling, scalable synthesis, and seamless integration into complete cells. These aspects, along with developments across other electrode materials, will be examined in the following sections.

2.1.1. P2-type layered cathodes. P2-type layered oxides in SIBs are defined by favourable two-dimensional diffusion pathways and moderate operating voltages, yet they face significant challenges due to Jahn–Teller distortions arising from Mn^{3+}, which induce lattice instability and lead to progressive capacity fading during cycling.[45] In order to address this issue, research has focused on multi-component systems such as $Na_{2/3}[Mn_{2/3}Ni_{1/3}]O_2$, where nickel functions both as a high-potential redox centre and as a stabiliser, mitigating Mn^{3+}-induced distortions through charge compensation.[11] These compositions have demonstrated improved capacity retention, maintaining around 80.8% after 500 cycles, and offer theoretical capacities of nearly 167 mAh g^{-1}. Nonetheless, preserving structural integrity under high-rate conditions remains challenging, as mechanical strain and phase transitions continue to affect electrochemical performance.

Doping has emerged as a central strategy for enhancing the stability and electrochemical behaviour of P2 cathodes. Beyond local lattice instabilities such as Jahn–Teller distortions, P2-type materials also face challenges from crystallographic phase transitions, particularly the P2 to O2 transition during deep sodium extraction, which involves slab gliding and rearrangement of the oxygen sublattice.[47] These transformations often

lead to irreversible structural changes and capacity loss. Lithium doping has proved particularly effective, substituting lithium for transition metals typically promoting a solid-solution reaction pathway that suppresses such phase transitions and limits volume variation during cycling. For instance, Li-doped $Na_{0.67}Li_{0.12}Ni_{0.2}Mn_{0.6}O_2$ exhibits significant structural stability upto 100 cycles.[13] Solid-state NMR studies confirm that lithium incorporation stabilises local TM-oxygen bonding environments, thereby enhancing electrochemical performance. Beyond lithium, dopants such as magnesium[48] and iron[49] have also been explored for their ability to reinforce lattice stability, though they generally exert subtler effects and do not significantly alter redox mechanisms.

As discussed earlier, when sodium is extracted from the P2 lattice during charging, the resulting electrostatic repulsion between adjacent TM layers can destabilize the structure, leading to a phase transformation into the less desirable OP4/Z phase.[49] However, researchers discovered that when a small amount of potassium, an ion significantly larger and more sluggish than sodium was introduced ideally at the prismatic sodium sites, significant changes to the phase evolution were noted.

In the resulting compound, $Na_xK_{0.065}MnO_2$, the hypothesised immobile potassium ions lodged themselves between the TM layers in the Na_e position, acting as rigid structural pillars (Fig. 3b).[12] Their presence suppressed the lateral gliding of the layers and effectively reinforced the lattice. This subtle yet profound modification allowed for the reversible extraction and reinsertion of as many as 0.901 sodium-ions per formula unit without inducing any significant structural collapse. The outcome was a cathode capable of delivering a reversible capacity of 240.5 mAh g^{-1}.[12] Further structural refinement techniques confirmed that this potassium-doped material experienced nearly 30% less lattice changes during cycling compared to its undoped counterpart. The challenge in such doping studies, with low concentrations of dopants, is to conclusively understand the location and distribution of the dopant, *i.e.*, whether the dopant is located in an ordered manner in the crystal structure, disordered and present on the surface of the particles.

An additional challenge in P2-type cathodes is sodium-vacancy ordering, particularly pronounced at intermediate states of charge due to the prismatic coordination of sodium ions. Sodium-vacancy ordering induces local lattice distortions, hinders sodium mobility, and contributes to capacity fading. Strategies to mitigate sodium-vacancy ordering include nano-engineering, core–shell architectures, and compositional tuning. For instance, adjusting nickel content from $Na_{2/3}Ni_{0.3}Mn_{0.7}O_2$ to $Na_{2/3}Ni_{1/3}Mn_{2/3}O_2$ produces zigzag Na^+/vacancy arrangements that enhance ion transport and cycling stability.[14] Doping with lithium[15] or niobium[50] has also proved effective in modifying atomic-scale ordering and improving sodium-ion diffusion, particularly under low-temperature conditions. Distinguishing between ordering patterns intrinsic to as-

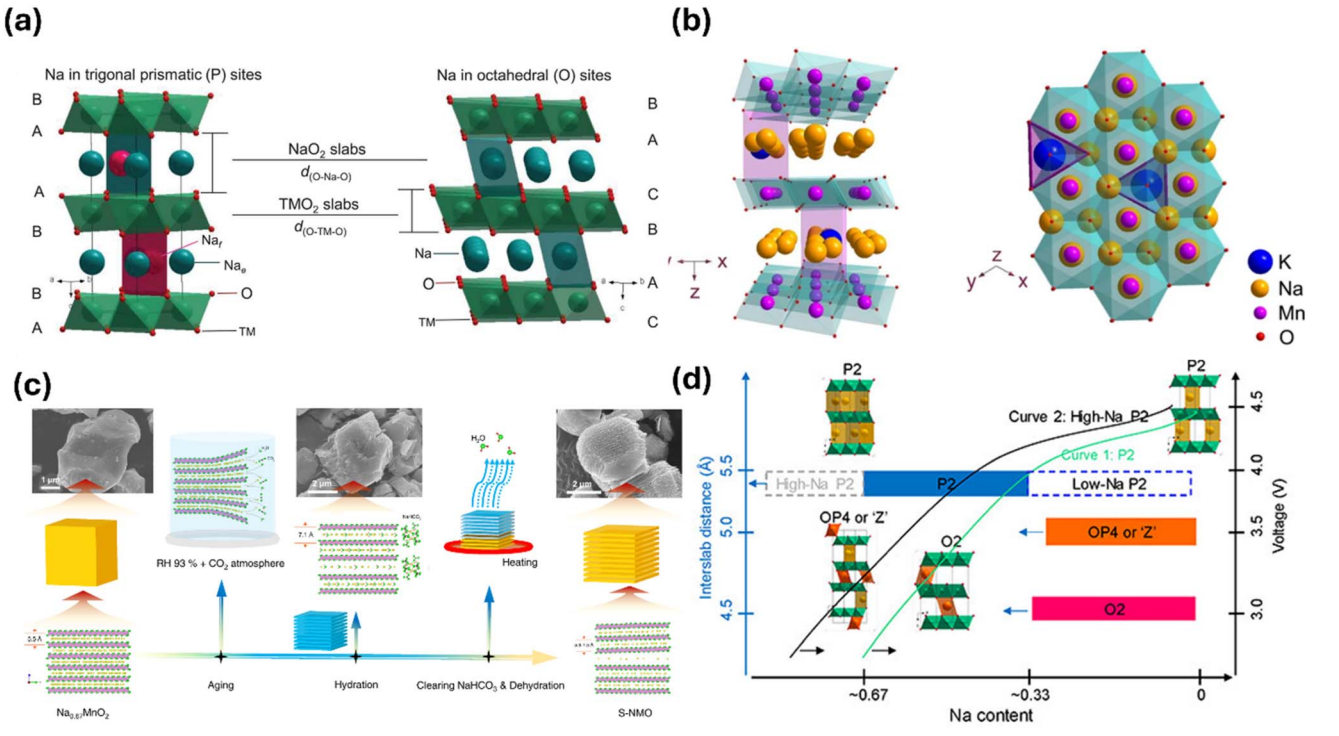

Fig. 3 (a) Prismatic and octahedral arrangement of sodium in layered cathode. Reproduced from ref. 14 with permission from AAAS, copyright 2020. (b) Structure of K doped $NaMnO_2$, K^+ was found to be most stable in the Na_e position. Reproduced from ref. 12 with permission from Springer Nature, copyright 2021. (c) Schematic illustration of the preparation process of hydrated $Na_{0.67}MnO_2$. Reproduced from ref. 12 with permission from Springer Nature, copyright 2021. (d) Phase transitions in high sodium content P2. Reproduced from ref. 47 with permission from American Chemical Society, copyright 2020.

synthesised materials and dynamic rearrangements during cycling remains critical, increasingly relying on advanced characterisation techniques.

P2 cathodes are also notably sensitive to atmospheric exposure. Compounds in this class readily absorb moisture, transforming into hydrated phases such as birnessite or buserite.[51] These transformations promote surface reactions with carbon dioxide, leading to the formation of hydroxides and carbonates that consume active material and reduce capacity. Traditionally regarded as a contaminant, moisture reacts with sodium-based cathodes to form surface carbonates, blocking active sites and limiting performance. However, in a bold reversal of convention, researchers adopted a water-mediated strategy to improve not degrade the cathode properties.

By aging $Na_{0.67}MnO_2$ in a water and CO_2 containing (aqueous) environment for six days, they encouraged moisture to infiltrate the layers and expand the lattice along the stacking axis from 11 to 14.2 Å (Fig. 3c).[52] This hydrated structure facilitated easier sodium migration and significantly improved cycling stability. Notably, the hydrated cathode retained 98.7% coulombic efficiency over 500 cycles while delivering a capacity of 150 mAh g^{-1} in the 2–4 V range. Even more interesting, the observed near-zero-strain intercalation behaviour was not confined to manganese-rich systems. The same approach, when applied to $Na_{0.67}Zn_{0.1}Mn_{0.9}O_2$ and $Na_{0.67}Fe_{0.1}Mn_{0.9}O_2$, yielded similarly promising results, suggesting a broader applicability of water-mediated layer engineering.[52]

Despite this success, the P2-type structure has historically suffered from a fundamental limitation: a relatively low average redox potential. This restricts the energy density of the battery, particularly when operating in conventional voltage windows. Researchers tackled this issue by investigating how the electronic environment of the TM–O bonds could be tuned to elevate redox activity.[47] Central to their hypothesis was the idea that hybridised TM–oxygen orbitals must be kept at higher energy levels to participate effectively in charge transfer. To do that, TM ions valency must be kept low, something that can be achieved by increasing the sodium content in the structure.

However, sodium content alone isn't enough. The spacing between TM layers plays a crucial role in stabilising additional sodium ions in the prismatic sites. In $Na_{0.85}Li_{0.08}Ni_{0.30}Mn_{0.62}O_2$, a reduced interlayer distance helped accommodate more sodium and, consequently, more electrons (Fig. 3d). Compared to a typical P2 cathode like $Na_{0.67}Li_{1/12}Ni_{1/4}Mn_{2/3}O_2$, which operated with a TM oxidation state of +3.33 and delivered 82 mAh g^{-1}, the higher-sodium-content variant had a lower oxidation state of +3.167 and yielded over 100 mAh g^{-1} in the same voltage range (2–4 V).[47] This subtle shift in electronic structure opened up greater redox participation and higher capacity without sacrificing structural integrity.

Yet structural degradation looms large in P2 materials, particularly when more than two-thirds of the sodium is removed from the host framework. As sodium content drops below 33%, the P2 structure becomes increasingly unstable, eventually transforming into the O2 phase. Interestingly, while such transitions are even more abrupt in O3-type materials, the need to delay or prevent phase change remains a shared challenge across both structures.

Here again, potassium appeared to prove its worth. In a separate study, researchers synthesised a precursor compound using a solid-state route. By constructing a half-cell with a sodium metal counter electrode, they enabled a staged exchange: during the first discharge, 0.441 units of sodium were inserted, and during the first charge, most of the potassium was removed, leaving behind a stable composition of $Na_xK_{0.08}[Ni_{0.2}Mn_{0.8}]O_2$.[17] This post-synthetic configuration successfully suppressed the P2-to-O2 phase transition even at low sodium contents, and the material delivered a high capacity of 194 mAh g^{-1} at 0.1 C. Once again, potassium played the quiet but crucial role of structural "guardian", maintaining interlayer spacing and permitting efficient sodium diffusion.

While considerable progress has been made in developing and stabilising P2-type layered cathodes, achieving commercial viability still depends on further improvements in cycling durability, air stability, and scalable synthesis techniques. The interplay between crystallographic phase transitions, local distortions, electrochemical processes, and cycling performance continues to drive active research in this important area of SIB development.

2.1.2. O3-type layered cathodes. A representative O3-type layered oxide is O3–$NaNi_{1/3}Fe_{1/3}Mn_{1/3}O_2$, which delivers specific capacities between 140 and 160 mAh g^{-1}, coupled with excellent capacity retention of around 95% over several hundred cycles within a voltage window of 2 to 4 V.[53] The compositional synergy in this material leverages the high redox potential of nickel, the structural stabilising role of manganese, and the contribution of iron to cycling durability. Nonetheless, the practical deployment of O3-type cathodes remains hindered by several inherent limitations.

A primary challenge lies in the sluggish kinetics of sodium-ion migration. Unlike the open prismatic channels in P2-type structures, O3-type materials require sodium ions to intercalate narrow bottlenecks between adjacent octahedral sites. This structural constraint hinders ion diffusion, resulting in poor rate capability and reduced cycling stability, particularly under high-current conditions. Furthermore, O3 structures are susceptible to phase transitions during deep desodiation, such as transformations to P3 or O′3 phases, which introduce lattice strain and lead to structural degradation.

Considerable research has been directed towards overcoming these obstacles through compositional modification. Cation doping with larger ions, including Ca^{2+},[20] Ti^{4+},[54,55] and rare-earth elements like La^{3+},[56] and Ce^{4+},[57] has been shown to expand interlayer spacing (Fig. 4a). This adjustment facilitates Na^+ diffusion and helps suppress undesirable phase transitions. For example, La doping on the transition metal site in O3-type systems has improved capacity retention from 63% to 80% after 500 cycles, highlighting the potential of interlayer engineering to stabilise structural evolution.[58]

Morphological engineering has also emerged as a valuable strategy for performance optimisation. Techniques such as nanostructuring and single-crystal synthesis can shorten sodium-ion diffusion paths and mitigate adverse grain

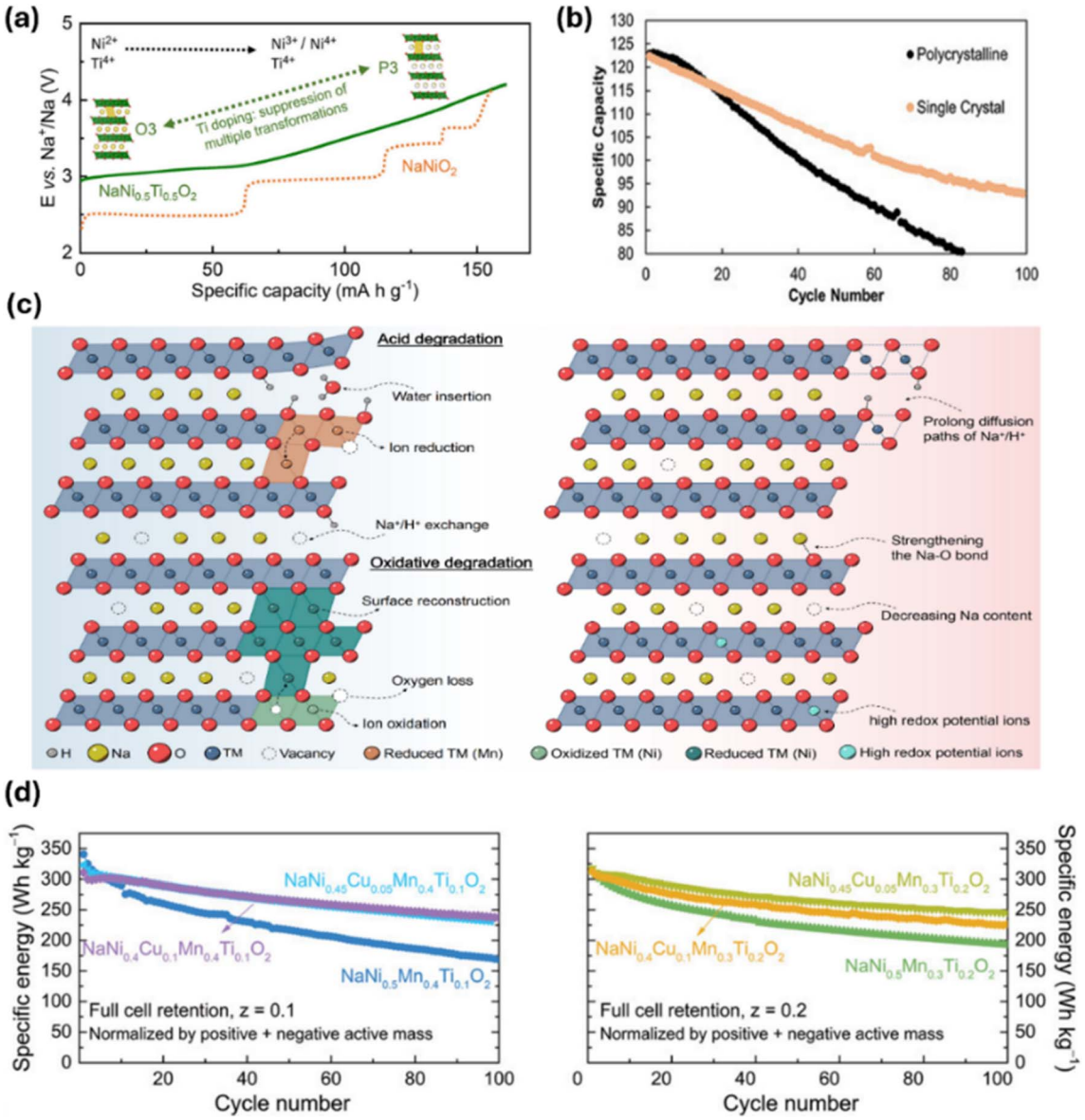

Fig. 4 (a) The effect of Ti doping on structural evolution, as demonstrated by charge–discharge profiles. Reproduced from ref. 56 with permission from American Chemical Society, copyright 2019. (b) Impact of single-crystal morphology on cycling stability, as demonstrated by cycling performance. Reproduced from ref. 59 with permission from Wiley-VCH GmbH, copyright 2022. (c) Schematic illustration highlighting the key factors affecting air stability in layered sodium cathode materials. Reproduced from ref. 60 with permission from Elsevier, copyright 2024. (d) The influence of Cu/Ti doping on long-term stability in a full-cell configuration. Reproduced from ref. 61 with permission from Wiley-VCH GmbH, copyright 2019.

boundary effects, which can elevate internal resistance.[62] Recent progress in promoting preferential platelet growth has demonstrated that tailoring specific crystallographic orientations can further optimise ionic transport pathways by having crystal orientation parallel to Na diffusion channels, leading to improved cycling performance and structural resilience (Fig. 4b).[59]

Despite these advances, O3-type cathodes continue to face significant challenges related to air sensitivity. Their high sodium content makes them highly reactive to moisture, triggering spontaneous Na^+/H^+ exchange and subsequent proton ingress into the lattice (Fig. 4c).[59] These reactions can cascade into further side reactions involving CO_2 and O_2, ultimately causing lattice collapse, crack and Na_2CO_3 formation, and rapid capacity loss. To counteract this vulnerability, researchers have explored various dopants, including Ti^{4+},[60] Al^{3+},[63] Zn^{2+}, [64] and Cu^{2+},[22] to lower the ionic potential and strengthen Na–O bonding (Fig. 3d). For instance, Ti^{4+} doping reinforces the structural framework by enhancing O–Na bond strength, while Cu^{2+} doping elevates redox potentials and contributes to improved cycling stability.

To further address the air sensitivity and sluggish Na-ion kinetics typically associated with O3-type materials, a universal strategy based on sodium vacancy engineering was

introduced, or sodium-deficient O3-type materials. For example, $Na_{0.93}Li_{0.12}Ni_{0.25}Fe_{0.15}Mn_{0.48}O_2$ exhibits significantly improved air stability and electrochemical performance due to controlled Na-site vacancies.[65] These vacancies reduce the shielding effect of surrounding oxygen atoms, enhancing Na^+ mobility and suppressing surface degradation upon air exposure. Titration experiments after 48 h of ambient exposure revealed minimal alkali residue formation, confirming superior chemical stability. Furthermore, density functional theory (DFT) calculations showed a substantial reduction in the Na-ion migration barrier, from 1000 meV in a vacancy-free lattice to 300 meV in the vacancy-engineered structure. This optimisation not only increased the aged capacity retention from 84.9% to 95.9% but also improved high-rate capacity retention from 54.7% to 70.8%, demonstrating the efficacy of vacancy engineering in enabling air-stable, high-rate O3 cathodes.

Recent research on O3-type layered oxides has revealed the critical role of anionic redox activity in enhancing the energy density of SIBs. A key breakthrough was demonstrated in the fully sodium-stoichiometric $NaLi_{1/3}Mn_{2/3}O_2$, where lithium substitution unlocked reversible oxygen redox chemistry.[22] Li doping in the TM layers induced distinct structural and electronic effects. Due to the smaller ionic radius of lithium-ions (0.76 Å) compared to Mn^{3+}/Mn^{4+} (0.65–0.58 Å), the local coordination environment of the TM–oxygen lattice is altered, leading to weakened hybridisation between O 2p and Mn d-orbitals. This destabilisation of oxygen electronic states lowers the energy required for oxygen participation in redox processes ($O^{2-} \rightarrow O^{n-}$, $n < 2$), as evidenced by X-ray absorption spectroscopy and resonant inelastic X-ray scattering. Additionally, Li substitution enhances lattice flexibility, facilitating Na^+ extraction while stabilising the desodiated structure. Consequently, a dual cationic (Mn^{3+}/Mn^{4+}) and anionic (O^{2-}/O^{n-}) redox mechanism is achieved, delivering a high reversible capacity of 190 mAh g^{-1} at a current rate of C/8.

Beyond Li substitution and vacancy design, understanding and controlling anionic redox chemistry has been crucial for improving O3-layered oxides. Researchers systematically investigated the anionic redox behaviour in $NaMn_{1/3}Fe_{1/3}Ni_{1/3}O_2$ and confirmed that oxygen actively participates in reversible charge compensation within the 4.0–4.3 V window without triggering irreversible oxygen loss.[22] To enhance anionic redox while mitigating structural degradation, they employed a synergistic strategy combining Zr^{4+} doping with a conformal ZrO_2 surface coating. Zr^{4+} substitution modulated the Na–O–TM local structure by shortening TM–O bonds, expanding Na-layer spacing, and raising the energy of O-2p states toward the Fermi level, thereby facilitating electron removal from oxygen. Simultaneously, the ZrO_2 coating suppressed electrolyte-induced surface corrosion and reduced gas evolution. This dual modification lowered the Na-ion migration barrier (from 0.61 eV to 0.53 eV), stabilised O3 $\leftrightarrow$ P3 phase transitions, and improved both rate capability and cycling stability, achieving 160 mAh g^{-1} with >80% capacity retention after 100 cycles at 1 C. This work provides direct mechanistic insights into oxygen redox participation and demonstrates a generalised approach to simultaneously tuning anionic redox and structural robustness.

In addition to cation substitution and coating strategies, high-voltage stabilisation of O3-type oxides was achieved through a dual Sn-modification approach.[66] In $NaNi_{1/3}Fe_{1/3}Mn_{1/3}O_2$, Sn^{4+} ions substituted TMs in the bulk lattice, reinforcing the TM–O framework and suppressing detrimental cation migration that typically triggers irreversible O3 $\rightarrow$ P3′ transitions above 4.0 V. Simultaneously, a thin Sn/Na/O nanolayer formed on the particle surface during synthesis, mitigating parasitic side reactions with the electrolyte. Importantly, this dual modification was accomplished in a single scalable step, avoiding complex multi-stage treatments. As a result, the optimised 8% Sn-modified cathode exhibited a higher reversible voltage limit (4.1 V), an initial discharge capacity of 126.9 mAh g^{-1} at 0.1 C, and good cycling stability with 70% retention after 150 cycles at 0.5 C. Full-cell configurations with hard carbon anodes further confirmed strong practical potential, delivering 81% retention after 200 cycles.

Although significant progress has been made, O3-type layered cathodes remain constrained by kinetic limitations and environmental instability. Further optimisation and deeper understanding of the interplay between compositional design, lattice dynamics, and environmental resilience will be crucial for unlocking the full commercial potential of O3-type cathodes in SIBs.

2.1.3. P2/O3 biphasic layered cathodes. In the search for cathode materials that combine high energy density with robust cycling stability, considerable attention has turned to P2/O3 biphasic layered systems. These hybrid materials are designed to integrate the rapid sodium-ion diffusion of P2-type frameworks with the higher sodium content and energy density intrinsic to O3-type phases, thereby harnessing the strengths of both structures while mitigating their individual limitations (Fig. 5a–c). P2 phases provide broad diffusion channels, enabling excellent rate capability and lower diffusion barriers for sodium ions. By contrast, O3 phases offer higher sodium content and increased theoretical capacities but suffer from narrower ionic pathways and greater sensitivity to atmospheric exposure. Combining both phases within a single cathode creates interfacial regions that act as mechanical buffers during sodium-ion insertion and extraction, helping to relieve stress, suppress crack formation, and enhance cycling stability and electrochemical performance.

Experimental studies reveal that the electrochemical behaviour of P2/O3 biphasic cathodes is highly sensitive to the proportion of each phase.[23] Such balanced phase compositions have delivered significant improvements in capacity retention and rate performance, positioning biphasic systems as strong contenders for high-voltage SIBs.

Nonetheless, the integration of P2 and O3 phases introduces intrinsic challenges. Differences in lattice parameters and crystal symmetries can lead to interfacial strain, lattice mismatch, and mechanical instability during charge–discharge cycling. These effects contribute to microcrack formation, phase segregation, and elevated interfacial resistance, undermining the structural integrity and electrochemical performance of the material. Achieving precise control over phase distribution, crystallographic orientation, and interfacial

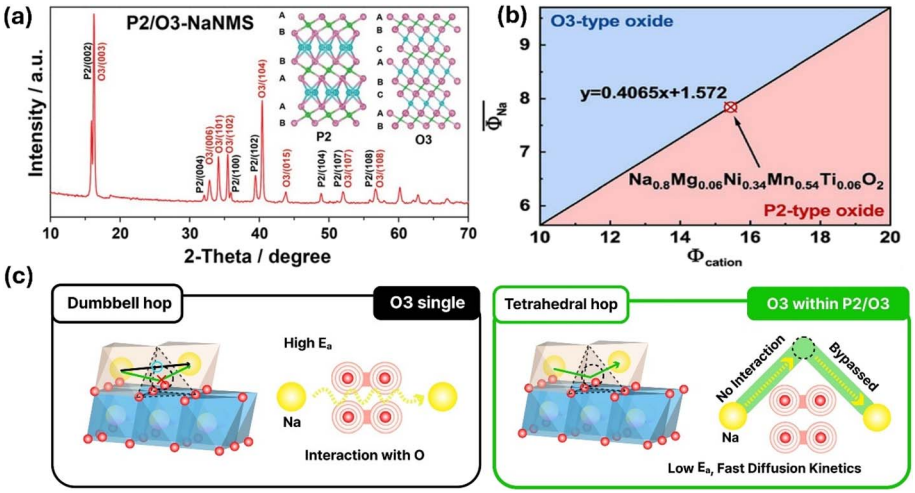

Fig. 5 (a) X-ray diffraction analysis of biphasic P2–O3. Reproduced from ref. 23 with permission from Wiley-VCH GmbH, copyright 2022. (b) Design principle of P2–O3 biphasic cathode. Reproduced from ref. 67 with permission from Wiley-VCH GmbH, copyright 2025. (c) Sodium movement in O3 type and P2–O3 type. Reproduced from ref. 68 with permission from Wiley-VCH GmbH, copyright 2025.

chemistry is therefore critical for the practical implementation of biphasic cathodes.

To rationally design P2/O3 biphasic cathodes, Maughan *et al.* moved beyond simply altering Na content and established a predictive relationship that allows control of the P2/O3 phase ratio *via* the composition of the TM layer.[31] They compared the previously proposed cationic potential and the average TM ionic radius as predictors and introduced a new parameter, the Radial Potential, defined as:

$$\text{Radial potential} = (\text{average TM-radius} \times \text{weighted Na-potential})/\text{weighted oxygen potential})$$

They found a strong correlation between radial potential and the P2 phase fraction: a smaller radial potential yields higher P2 content, while a larger radial potential favors O3-rich phases. Importantly, this predictor is method-dependent, as different synthesis routes (sol gel *vs.* solid-state) shift the P2/O3 ratio. The authors proposed a three-step design strategy: (1) use cationic potential to locate compositions near the P2/O3 phase boundary, (2) fine-tune the ratio using radial potential, and (3) adjust synthesis route and conditions (temperature, calcination time) for additional control.

They also noted exceptions, dopants like Mg and Zn deviate from the predicted trend due to superlattice formation in P2 regions, altering phase stability. Finally, they demonstrated that tuning the P2/O3 ratio tailors' electrochemical properties. P2-rich phases such as $Na_{0.72}Mn_{0.4}Fe_{0.4}Ti_{0.1}Cu_{0.1}O_2$ showed superior rate capability and cycling stability, while O3-rich phases such as $Na_{0.75}Mn_{0.4}Fe_{0.4}Ti_{0.1}Al_{0.1}O_2$ delivered higher energy density.

A biphasic layered oxide cathode material $Na_{0.8}Mg_{0.06}Ni_{0.34}Mn_{0.54}Ti_{0.06}O_2$ was synthesised *via* solid-state reaction by sintering at temperatures ranging from 800 °C to 1000 °C to investigate the thermodynamic formation and evolution of P2/O3 biphasic structures.[32] X-ray diffraction analysis revealed that the sample sintered at 800 °C exhibited a biphasic nature, containing both P2 and O3 phases, with the P2 phase characterised by a (002) reflection and the O3 phase by a (003) reflection. As the sintering temperature increased, a systematic phase transformation from P2 to O3 was observed, with the P2 phase gradually diminishing. At 1000 °C, the sample showed a pure O3 phase, indicating that higher temperatures thermodynamically favors O3-type crystallisation.

Quantitative Rietveld refinement showed that the O3 phase content increased from 42.75% at 800 °C to 100% at 1000 °C, while the P2 content reduced accordingly. This transformation is accompanied by enhanced structural stability, especially at intermediate temperatures. The sample sintered at 950 °C was described to display the optimal balance of P2 (24.3%) and O3 (75.7%) phases, minimal residual alkali content (2.8 wt%), and shorter TM–O bonds, leading to better crystallinity and sodium-ion transport properties.

Electrochemically, the sample sintered at 950 °C exhibited superior rate performance and cycling stability, delivering a high discharge capacity of 154.5 mAh g^{-1} at 0.1 C and retaining 87.25% of its capacity after 100 cycles at 1 C, corresponding to an energy density of 534 Wh kg^{-1}. This highlights that the controlled formation of biphasic P2/O3 domains, guided by thermodynamic factors such as sintering temperature and residual alkali content, offers a pathway to design high-rate, high-energy sodium-ion cathodes.

Addressing a separate but related challenge, Li *et al.* targeted the issue of Jahn–Teller distortions associated with Mn^{3+}/Mn^{4+} redox.[33] They developed a $Na_{0.8}Ni_{0.23}Fe_{0.34}Mn_{0.43}O_2$ cathode with a dominant O3 structure incorporating embedded P2 lamellae and demonstrated with the help of transmission electron microscopy that the intergrowth of P2 and O3 domains can mitigate long-range Jahn–Teller ordering.

The interfaces between O3 and P2 phases are thought to act as strain buffers, suppressing the cooperative alignment of distorted MnO_6 octahedra and thus preventing bulk structural collapse. This biphasic strategy effectively limits the Jahn–Teller

induced phase transitions that often destabilise Mn-rich O3 cathodes. Moreover, the presence of P2 domains improves the air stability of the material. The interfacial interactions between P2 and O3 phases restrict spontaneous deintercalation of Na^+ under ambient conditions, which is a known drawback of pure O3 structures due to surface instability. Electrochemically, the $Na_{0.8}Ni_{0.23}Fe_{0.34}Mn_{0.43}O_2$ cathode delivered an impressive initial discharge capacity of 146.4 mAh g^{-1} at 0.1 C, and retained a coulombic efficiency of 93.1% even after 200 cycles at 1 C. The enhanced performance was attributed to the stabilised Mn redox activity and reduced internal stress at phase interfaces, promoting a reversible and stable sodium extraction/insertion process.

To stabilise P2/O3 biphasic systems, various compositional engineering strategies have been explored. Doping with elements such as Ti, Cu, Mg, and Li has been shown to promote controlled phase coexistence, improve sodium-ion mobility, and suppress degradation pathways.[67] Doping with elements like Nb has also been linked to electronic structure modulation, narrowing the band gap and promoting more uniform sodium-ion diffusion throughout the lattice.[50]

Beyond compositional tuning, defect engineering including the introduction of oxygen and TM vacancies has been investigated as a route to enhancing structural stability and optimising electrochemical performance. However, it is understood that excessive vacancy creation can undermine lattice integrity and accelerate capacity fade. It is also often difficult to conclusively quantify the presence and amount of such vacancies. Emerging studies also highlight that even small variations in synthesis parameters, such as annealing temperatures and cooling rates, can significantly affect phase purity and interfacial properties in biphasic materials.

While P2/O3 biphasic cathodes represent a promising pathway for achieving balanced electrochemical performance in SIBs, substantial challenges remain in mastering interfacial engineering, scaling synthesis processes, and ensuring long-term stability under practical conditions. Comparatively, P2/P3 and P3/O3 systems may offer similar synergistic potential but remain underexplored due to synthetic complexity, highlighting the broader need for integrated experimental-computational methodologies in advanced cathode discovery.[68] Nevertheless, ongoing advances in compositional design, defect management, and process optimisation offer considerable promise for unlocking the full potential of these hybrid cathode configurations.

Building on this concept, Chen *et al.* introduced a biphasic $Na_{0.67}Li_{0.11}Fe_{0.36}Mn_{0.36}Ti_{0.17}O_2$ material *via* a high-ratio Li/Ti co-substitution strategy.[69] This design not only induced a well-defined P2/O3 phase interface but also enabled the activation of reversible oxygen redox reactions, contributing significantly to an high reversible capacity of 235 mAh g^{-1}, the highest among reported Fe/Mn-based layered oxide cathodes. Detailed structural analysis revealed a unique intersected interface between P2 and O3 phases, which played a crucial role in suppressing the P2 → OP4 transformation and reducing lattice mismatch stress during cycling. Consequently, the material delivered excellent cycling performance, retaining 85.4% of its capacity after 100 cycles, and showed limited Mn dissolution and microcrack formation. These findings underscored the value of combining chemical substitution with intelligent interface engineering to stabilise high-capacity sodium cathodes.

Further pushing the boundary, Zhou *et al.* explored the development of a high entropy, F-doped biphasic cathode with the apparent composition $Na_{0.7}Mn_{0.4}Ni_{0.3}Cu_{0.1}Fe_{0.1}Ti_{0.1}O_{1.95}F_{0.1}$.[70] By carefully optimising the P2 : O3 phase ratio (23 : 77), they achieved good electrochemical performance over a wide temperature range (−40 °C to 50 °C). The material exhibited a near-theoretical initial coulombic efficiency (ICE) of 97.6%, a stable discharge capacity at high current rates (86.7 mAh g^{-1} at 800 mA g^{-1}), and an energy density of 268 Wh kg^{-1} in full-cell configurations. *In situ* X-ray diffraction analysis and DFT simulations revealed a reversible P2/O3 → P3/OP4 evolution mechanism and low sodium-ion diffusion barriers, contributing to the cathode's excellent thermal and cycling stability. The work clearly demonstrated that high entropy doping, coupled with controlled phase distribution, can yield cathodes suitable for real-world applications under extreme conditions. It is however important to note that differentiating between F and O is extremely complex with many techniques at researchers' disposal. These elements have very similar scattering cross-sections in X-ray and neutron diffraction making it complex to distinguish them. Therefore, it is important to note the synthetic or anticipated composition and that the final product may be slightly different, *e.g.*, F-based surface species rather than incorporated into the crystal structure.

In comparing these studies, several shared strategies emerge. All three employed multi-element doping, often referred to as high entropy design to enhance structural integrity and suppress detrimental phase transitions. The introduction of F or Li/Ti played pivotal roles in activating oxygen redox or optimising sodium ion mobility. Moreover, careful engineering of the P2/O3 interface—either by phase ratio control or unique interfacial architectures—was essential in minimising internal stress and improving electrochemical reversibility. Collectively, these approaches enabled cathodes to simultaneously achieve high capacity, high ICE, and long-term stability, characteristics that were previously mutually exclusive in single-phase systems.

While these advances are promising, several challenges remain. Scaling the synthesis of such complex biphasic materials for commercial production requires precise control over doping levels and phase purity. Furthermore, although some full-cell demonstrations have been reported, more work is needed to evaluate the long-term compatibility of these cathodes with practical anode materials and electrolytes under commercial operating conditions. Finally, a deeper understanding of the interfacial dynamics between P2 and O3 phases, particularly under prolonged cycling or thermal stress, will be key to fully optimising these materials.

2.2. Polyanionic compounds

Polyanionic compounds have emerged as a prominent class of cathode materials for SIBs, valued for their structural

robustness and strong inductive effects. Unlike layered oxides, which often undergo phase transitions and lattice degradation during deep sodium extraction, polyanionic cathodes exhibit exceptional thermal stability and structural integrity. The incorporation of polyanionic groups such as PO_4^{3-} or SO_4^{2-} elevates the redox potential of transition-metal centres *via* inductive effects, enabling higher operating voltages and enhanced long-term cycling performance.[71]

Among these, sodium vanadium phosphate (NVP) with a NASICON-type framework has attracted sustained interest. Its three-dimensional network of VO_6 octahedra and PO_4 tetrahedra enables fast sodium-ion transport, while vanadium offers multiple redox states. The V^{3+}/V^{4+} redox couple, operating near 3.35 V, delivers reversible capacities of approximately 110 mAh g^{-1} with excellent cycling retention.[71] Efforts to exploit the higher-voltage V^{4+}/V^{5+} redox couple have been hindered by lattice instability and irreversible phase transitions, leading to capacity fading. Partial substitution of vanadium with iron has been explored to address these challenges, though fully stabilising the structure while activating multi-electron reactions remains unresolved.

Iron-based polyanionic compounds offer a more cost-effective and environmentally benign alternative to vanadium-based systems. NASICON-type $Na_3Fe_2(PO_4)_3$ possesses an open framework suitable for sodium-ion transport but is constrained by the modest voltage of the Fe^{2+}/Fe^{3+} [71] redox couple, limiting energy density. To address this, recent studies have focused on activating higher-potential Fe^{3+}/Fe^{4+} redox reactions and exploring zero-strain frameworks such as $Na_4Fe_7(PO_4)_6$. The latter exhibits good cycling durability, near-zero volume change, and nearly 100% capacity retention over 1000 cycles, making it particularly attractive for applications prioritising cost efficiency and lifespan over energy density. The last year has seen an accelerated increase in the commercialisation of $Na_4Fe_3(PO_4)_2(P_2O_7)$ or NFPP with a number of cell manufacturers producing commercial cells and internally demonstrating good safety characteristics under abuse conditions, *e.g.*, nail penetration and overcharge. This type of material provides working voltages around 3.1 V with low volume change (<4%) and stable cycling performance. Research work on these materials has focused on synthesis of phase-pure and high-performance materials with minimal energy requirements. For example, work compared combustion with conventional solid-state synthesis and found that combustion synthesized NFPP used less energy to produce, could produce a pure material and one that retained 99.7% of its capacity at 0.1C after 100 cycles.[72]

Manganese-containing polyanionic cathodes are also under exploration, driven by the low cost and abundance of manganese.[73] Activation of the Mn^{2+}/Mn^{3+} redox couple typically results in operating voltages between 2.5 and 3.8 V. However, Mn-based systems are susceptible to Jahn–Teller distortions and structural degradation during cycling, particularly at higher voltages.[73] Strategies such as partial substitution with more stable transition metals have been pursued to mitigate these effects, yet achieving a durable high-capacity system remains a challenge.[74]

Despite their advantages in safety and thermal stability, polyanionic cathodes generally suffer from lower electronic conductivity and energy density compared to layered oxides. To address these limitations, approaches such as nanoscale engineering and conductive surface coatings have been employed to shorten ion diffusion paths and enhance electronic transport. Nonetheless, increasing surface area can also accelerate parasitic side reactions, necessitating careful control over particle morphology and synthesis conditions.

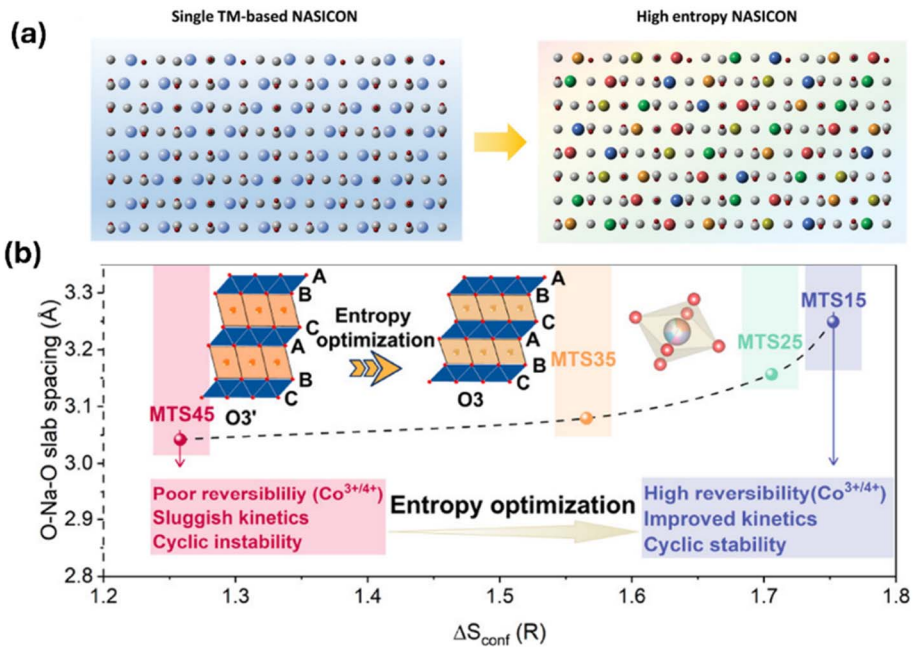

Fig. 6 (a) Design of high entropy NASICON. Reproduced from ref. 76 with permission from Wiley-VCH GmbH, copyright 2022. (b) High entropy optimisation in layered cathode. Reproduced from ref. 28 with permission from American Chemical Society, copyright 2023.

From a commercial standpoint, polyanionic cathodes are particularly well-suited to applications requiring high thermal stability and long cycle life, such as stationary grid storage. While they may not match layered oxides in terms of gravimetric and volumetric energy density, their inherent safety, chemical durability, and compositional flexibility make them strong candidates for cost-sensitive markets. Continued advances in multi-electron redox chemistries, novel framework design, and scalable synthesis are expected to further expand the role of polyanionic cathodes in the SIB landscape. The learnings from $LiFePO_4$ development in lithium-ion batteries can be applied and deployed in sodium-based systems.

2.3. High entropy cathodes

High entropy materials are generally defined as compounds composed of five or more principal elements in nearly equiatomic proportions. More specifically, a material can be classified as high entropy if its configurational entropy exceeds 1.5 R (where R is the gas constant).[75] The configurational entropy of a system is directly related to the mole fraction of its constituent elements; as the mole fraction increases, so does the configurational entropy (Fig. 6a and b). According to the Gibbs free energy equation, $dG = H - TdS$, where G represents Gibbs free energy, H is enthalpy, T is temperature, and S is entropy, an increase in entropy leads to a decrease in Gibbs free energy. This reduction in free energy enhances the thermodynamic stability of the material.

2.3.1. High entropy layered oxides. During the desodiation of layered sodium-ion cathodes, Na^+ ions are extracted from the structure, and to maintain charge neutrality, the TM ions are oxidised to higher valence states. In conventional O3-type layered oxides, typically containing two to four different TMs, the associated changes in ionic radii often induce significant local structural distortions. With fewer redox-active species, the responsibility of accommodating valence changes and associated strain falls on a limited number of cations, increasing the likelihood of irreversible phase transitions and structural collapse. This is also compounded by Na^+/vacancy ordering in the Na-rich layers.

In contrast, high entropy compositions, which incorporate a larger variety of TMs, enable these redox and strain effects to be distributed more evenly across the crystal lattice and in some cases reducing the barrier to overcome Na^+/vacancy ordering. This configurational diversity buffers the structure against abrupt distortions, thereby delaying or mitigating phase evolution. The first high entropy sodium cathode was reported with a nine-component system: O3–$NaNi_{0.12}Cu_{0.12}Mg_{0.12}Fe_{0.15}Co_{0.15}Mn_{0.1}Ti_{0.1}Sn_{0.1}Sb_{0.04}O_2$ (Fig. 7a).[34] In this design, Ni^{2+}, Cu^{2+}, Fe^{3+}, and Co^{3+} contributed to the capacity, while Mg^{2+} and Ti^{4+} served as structural stabilisers. Sn^{4+} and Sb^{5+} were introduced to raise the average voltage, and Mn^{4+} acted as a framework former. This material delivered an initial capacity of 110 mAh g^{-1} at 0.1 C (2.0–3.9 V) and retained 83% of its capacity over 500 cycles, highlighting the advantages of entropy-induced stabilisation.

Typically, O3-type layered cathodes undergo an O3 → P3 phase transition during desodiation *via* TM slab gliding. However, in the high entropy system, the phase evolution was modified to proceed through an intermediate O3′ phase, following an O3 → O3′ → P3 pathway during charging, and

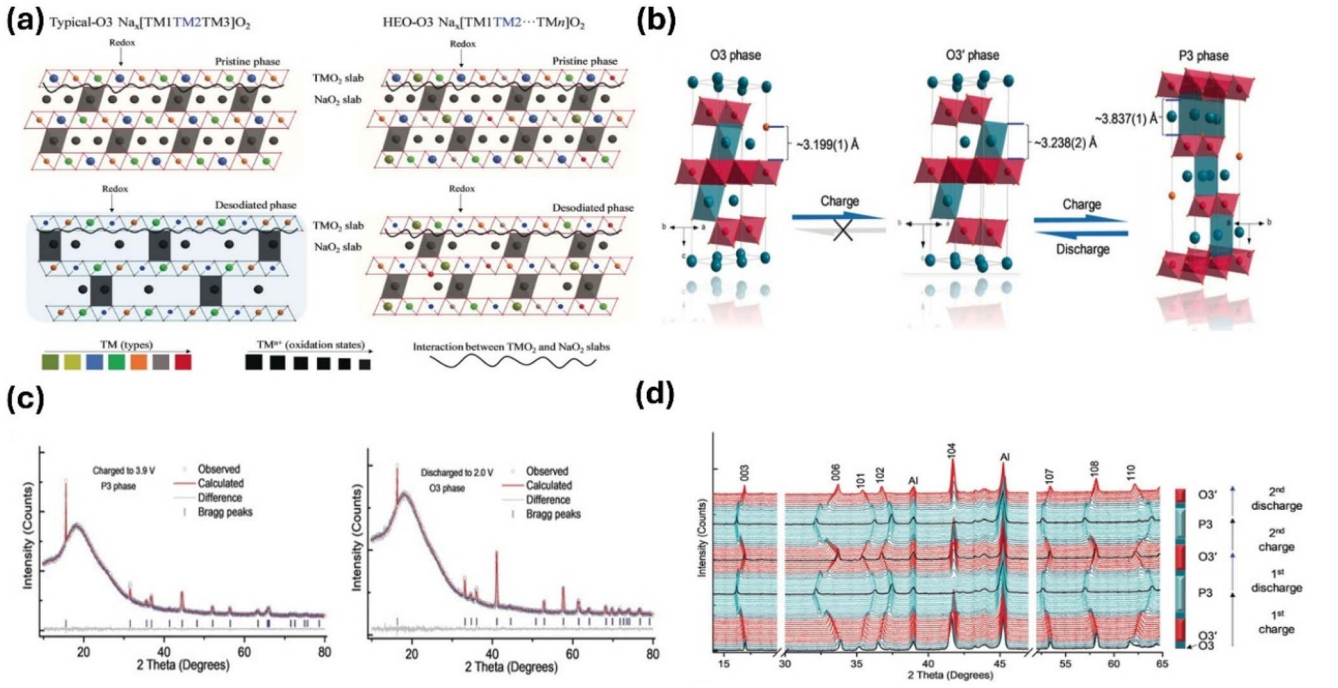

Fig. 7 (a) Generalised high entropy effects in layered cathodes. (b) Evolution of layered structure when an high entropy approach is used. (c) *Ex Situ* XRD analysis of $NaNi_{0.12}Cu_{0.12}Mg_{0.12}Fe_{0.15}Co_{0.15}Mn_{0.1}Ti_{0.1}Sn_{0.1}Sb_{0.04}O_2$. (d) *Operando* XRD patterns of $NaNi_{0.12}Cu_{0.12}Mg_{0.12}Fe_{0.15}Co_{0.15}Mn_{0.1}Ti_{0.1}Sn_{0.1}Sb_{0.04}O_2$. Reproduced from ref. 34 with permission from Wiley-VCH GmbH, copyright 2019.

reversibly during discharge (Fig. 7b). The O3′ phase retained the overall layered framework but exhibited modified lattice parameters due to Na extraction. This altered pathway effectively delayed the O3 → P3 transition, enhancing long-term cycling stability.

An entropy-tailored approach was further employed to control phase evolution and redox dynamics in Na-layered cathodes. Specifically, a high entropy cathode, $NaCu_{0.1}Ni_{0.2}Co_{0.2}Fe_{0.2}Mn_{0.15}Ti_{0.15}O_2$, was synthesised by substituting Cu, Co, and Ti into the parent $NaNi_{0.3}Fe_{0.4}Mn_{0.3}O_2$ system.[35] Although this composition showed a lower initial capacity (123.3 mAh g^{-1} at 0.1 C), it exhibited markedly improved capacity retention. At high states of charge (SOC > 4.1 V), the parent cathode suffered from voltage decay and capacity fading, attributed to irreversible oxygen redox and TM migration. These degradation pathways were effectively suppressed in the high entropy cathode, which displayed enhanced electrochemical stability and improved sodium-ion diffusion kinetics.

Operando X-ray diffraction analysis revealed reduced lattice parameter fluctuations in the high entropy samples compared to the parent, suggesting suppression of anisotropic strain and improved structural integrity (Fig. 7d). The irreversible redox activity in the parent system was attributed to the reduction of Ni^{4+} at high voltages, driven by O 2p to Ni 3d electron transfer. This behaviour was substantially mitigated in the high entropy composition, as evidenced by its more reversible redox response. Oxygen K-edge X-ray absorption spectroscopy further confirmed lower oxygen redox activity in the high entropy material, indicated by decreased spectral intensity compared to the undoped counterpart.

High entropy systems rely on a balance between redox-active cations for charge compensation and redox-inert cations for structural stability. While numerous studies highlight improved structural resilience due to configurational entropy, the mechanistic understanding remains limited. Wang *et al.* addressed this by investigating a compositional series of O3-type $Na_{0.83}Li_{0.1}Ni_{0.25}Co_{0.2}Mn_xTi_xSn_{0.45-2x}O_{2-\delta}$, where Mn, Ti, and Sn were varied to tune entropy.[35] Increasing the content of inert cations such as Mn and Ti enhanced Na^+ kinetics by delocalising electron density and weakening Na–O bonding. As entropy increased, the thickness of the alkali layer expanded, while the transition metal layer contracted along the (00l) direction. This structural modulation correlated with improved coulombic efficiency and diffusion kinetics.

Overall, high entropy strategies present a powerful avenue to rationally engineer phase transitions, suppress degradation pathways, and enhance the long-term performance of sodium-ion cathodes. Future efforts should focus on quantifying the impact of configurational entropy from both structural and electronic perspectives, with particular emphasis on its role in redox dynamics, sodium-ion diffusion, and phase evolution under practical cycling conditions. It should be emphasised that structural and compositional characterisation post-synthesis and after electrode fabrication are key elements that need to be reported and validated.

2.3.2. High entropy polyanionic cathodes. The concept of utilising high entropy effects, initially explored in sodium-layered oxide cathodes, has shown potential in improving the performance of a range of battery materials. Building upon these developments, the first report on a high entropy polyanionic cathode appeared in 2022, marking a significant step forward in energy storage research.[77] This opened new avenues for enhancing the performance of polyanionic cathodes.

The activation of the V^{4+}/V^{5+} redox couple has been a primary challenge in the development of polyanionic sodium cathodes due to the inherent structural instability. However, recent advancements using high entropy NVP materials have demonstrated marked improvements.[78] A high entropy NVP, synthesised by partially substituting Cr, Fe, Mn, Mg, and Ca at the vanadium site, successfully activated the V^{4+}/V^{5+} redox couple while improving structural and electrochemical performance.[78] The compound, $Na_{3.32}V_{1.6}Cr_{0.08}Fe_{0.08}Mn_{0.08}Mg_{0.08}Ca_{0.08}(PO_4)_3$, was produced using a sol–gel method, and exhibited effective sodium storage capabilities.

The sodium storage mechanism in this high entropy NVP was investigated using *in situ* X-ray diffraction and X-ray absorption near-edge structure techniques, revealing a combination of solid-solution and biphasic transition reactions. Electrochemical analysis indicated an improved specific capacity of 152.3 mAh g^{-1} at a current density of 0.05 Ag^{-1}, which was attributed to the activation of the V^{4+}/V^{5+} redox couple. Furthermore, the material displayed excellent structural stability, retaining 93.1% of its capacity after 2000 cycles. For comparison, only 40% of coloumbic efficiency was retained after 450 cycles in the non-high-entropy NVP sample.

Further analysis of the oxidation states during cycling indicated that only vanadium and iron actively participated in the electrochemical processes, while dopants such as Mn, Mg, Ca, and Cr remained electrochemically inactive. This inactivity contributed to enhanced structural stability and minimised volume expansion (9.87%) during cycling, positioning high entropy NVP as a promising candidate for durable and high-performance SIBs.

In another example, Fe, Mn, Cr, and Ti were added into the NVP structure in equal molar concentrations to synthesise high entropy $Na_{3.4}Fe_{0.4}Mn_{0.4}V_{0.4}Cr_{0.4}Ti_{0.4}(PO_4)_3$.[76] The presence of multiple transition metals at the same concentration appeared to exert a synergetic effect on the electrochemical behaviour. The high entropy NVP was able to deliver a capacity of 163 mAh g^{-1} at 0.1 C and demonstrated enhanced structural stability. High entropy effects, induced by atoms of varying sizes were described to shift the lattice strain of the parent material. The intense lattice strain mitigated phase transitions or volume expansion/contraction of this cathode material especially at higher voltages. The study also synthesised multiple Fe, Mn, Cr, and V rich compositions and found that each element played a distinct role in enhancing performance. For instance, the iron redox couple aided in expanding the voltage window, while the presence of manganese improved capacity due to $Mn^{3+/4+}$ redox activity. The incorporation of chromium and titanium played crucial roles in enhancing rate performance and cycling stability respectively.[76] A systematic study of dopant types, concentrations and their roles in the electrochemical

performance parameters provides incredible insight into future rational materials design.

A high entropy NASICON structure with the formula $Na_3VAl_{0.2}Cr_{0.2}Fe_{0.2}In_{0.2}Ga_{0.2}(PO_4)_3$ was reported to be effective in reversibly tapping into $V^{4+/5+}$ redox.[37] High entropy NASICON exhibited minimal volume change during the insertion and extraction of sodium, which was correlated in the work to superior structural stability. Interestingly, all the TMs except vanadium were electrochemically inactive during cycling. The lack of involvement of these elements in the redox processes was thought to be responsible for minimal volume change (1.1%) during electrochemical process. Additionally, superior structural stability of the high entropy $Na_3VAl_{0.2}Cr_{0.2}Fe_{0.2}In_{0.2}Ga_{0.2}(PO_4)_3$ was attributed to the depression of local migration of vanadium to the sodium site near the discharged state. The activation energy for diffusion was also reduced, resulting in the fabricated SIB with the high entropy NASCION cathode achieving a discharge capacity of 83 mAh g^{-1} (0.1 C) even at −20 °C.[37] It is interesting to note the relationship between high entropy considerations and electrochemical performance at different temperatures.

To further enhance the performance of the $Na_4Fe_3(PO_4)_2P_2O_7$ polyanionic cathode, various metal substitutions—specifically Ni, Co, Mn, Cu, and Mg—at the iron site were investigated.[79] The resulting compounds, such as $Na_4Fe_{2.85}$(Ni, Co, Mn, Cu, Mg)$_{0.03}(PO_4)_2P_2O_7$, exhibited enhanced ionic conductivity due to an expansion in the unit cell. DFT analysis further revealed the metallic nature of the $Na_4Fe_{2.85}$(Ni, Co, Mn, Cu, Mg)$_{0.03}(PO_4)_2P_2O_7$ phase, where the increased electronic conductivity was attributed to the facilitated excitation of electrons into the conduction band in this high entropy mixed-polyanion system. These enhanced transport properties were reflected in the electrochemical performance, as the high entropy sample achieved a coulombic efficiency of 99.94%, compared to the pristine sample's significantly lower efficiency of 57.2%. It should be noted that determining whether 0.03 of a formula unit substitute into the crystal structure is at the limits of many diffraction techniques. There can be ambiguity to whether the elements reside on the surface of the particles, homogeneously or as clusters, or whether they are in the crystal structure. The advantage of larger doping ratios, 0.2 of a formula unit provides more confidence on the reliable substitution into the crystal structure.

$Na_4Fe_3(PO_4)_2P_2O_7$ is a promising cathode material due to its abundant and cost-effective raw materials. However, its practical application is limited by the slow kinetics of sodium ions and the formation of impurity phases, such as $NaFePO_4$, during synthesis.[72] To address these challenges, titanium substitution at the iron site has emerged as an effective strategy. Crystal structure analysis of titanium-doped samples has revealed the absence of impurity phases like $NaFePO_4$ and $Na_2Fe_2O_7$, which were present in the pristine sample. In the titanium-doped samples, the reduced iron content, in conjunction with the incorporation of titanium into the lattice, increased the system's entropy. This, in turn, lowered the Gibbs free energy, which the authors assign as the driving force for the formation of impurity-free $Na_4Fe_3(PO_4)_2P_2O_7$ phases. Beyond the elimination of impurity phases, titanium-doped samples also exhibited improved electrochemical behaviour and electronic conductivity. For instance, a coulombic efficiency of 86.9% was achieved after 1200 cycles at a 10 C rate. Meanwhile, the improvement in conductivity is attributed to the role of titanium in facilitating electron transport from the valence band to the conduction band, further improving the overall performance of the material.

Overall, high entropy doping in polyanionic sodium cathodes has emerged as an effective strategy to address long-standing challenges in this class of materials. The synergistic interaction among multiple transition metals in high entropy polyanionic compounds significantly enhances electrochemical kinetics, structural stability, and overall capacity.

2.4. Prussian blue and analogue compounds

Prussian blue analogues (PBAs) have emerged as one of the most promising families of cathode materials for SIBs, owing to their distinctive open-framework structures and their ability to reversibly intercalate sodium ions with minimal lattice strain.[80–83] PBAs possess a cubic lattice architecture in which TM centres are bridged by cyanide ligands, creating spacious

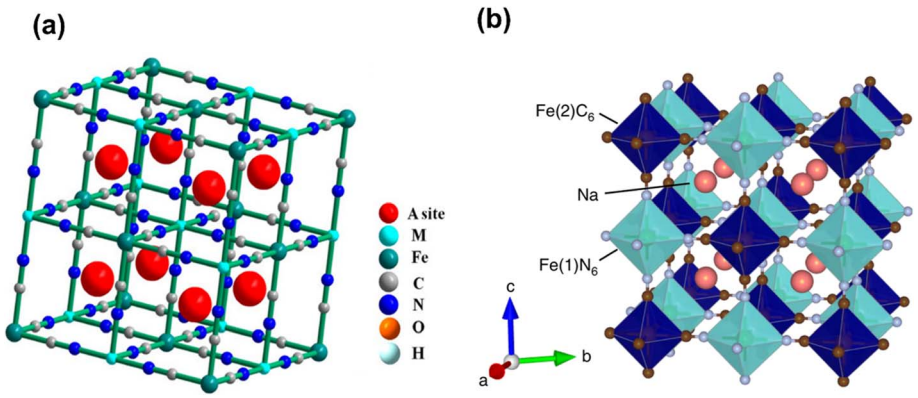

Fig. 8 Schematic illustration of a general (a) Prussian blue analogue (PBA), reproduced from ref. 81 with permission from American Chemical Society, copyright 2023 and (b) of $Na_{2-x}FeFe(CN)_6$, reproduced from ref. 80 with permission from Springer Nature, copyright 2020.

interstitial sites that facilitate rapid sodium-ion diffusion and support excellent rate capability (Fig. 8a).

Among the various PBAs, sodium iron hexacyanoferrate ($Na_2Fe[Fe(CN)_6]$) has drawn considerable attention due to its low cost, environmental benignity, and favourable operating voltage of around 3.4 *vs.* Na/Na^+.[84] It offers a high theoretical capacity exceeding 150 mAh g^{-1} and can be synthesised through relatively simple aqueous methods, making it an attractive candidate for large-scale applications.[82] Moreover, PBAs exhibit impressive structural stability during electrochemical cycling, delivering outstanding capacity retention even under high-rate conditions.

Despite these advantages, PBAs face inherent challenges that hinder their practical implementation. A major concern is the presence of coordinated and interstitial water molecules within the lattice, which can participate in undesired side reactions and reduce energy density.[85] Additionally, structural defects, particularly TM vacancies, can disrupt long-range crystallographic order and diminish reversible capacity. Indeed, many as-synthesised PBAs contain significant vacancy concentrations, leading to lower than theoretical capacities and compromised electronic conductivity.

Recent research has focused on overcoming these limitations through refined synthetic strategies. Techniques such as controlled precipitation, chelating agent-assisted synthesis, and post-synthetic treatments have effectively reduced vacancy content and minimised water incorporation, yielding materials with enhanced electrochemical performance.[85] Water-free PBAs have been successfully demonstrated, maintaining high capacities while suppressing side reactions during cycling.[86] Beyond ($Na_2Fe[Fe(CN)_6]$), mixed TM PBAs—including Co/Fe, Mn/Fe, and Ni/Fe systems—have been explored to tune redox potentials and optimise energy density.[87] For instance, partial substitution of Fe with Mn has been shown to raise the operating voltage, albeit sometimes at the cost of structural stability and long-term cycling performance.

One aspect that is often overlooked in the literature and reporting in general is the electrode structure and composition relative to the as-synthesised material. The electrode formulation chemistry in PBA-based systems is critical in conserving the structure of the PBAs on-electrode and hence being able to develop structure–property relationships with which to build rational design strategies.

From a commercial standpoint, PBAs are particularly well suited for stationary energy storage, where moderate energy density, low cost, and long cycle life take precedence over maximum energy density. Their straightforward and scalable aqueous synthesis offers notable manufacturing advantages compared to the more complex processing required for layered oxides and polyanionic materials. Nevertheless, achieving high volumetric energy density and fully resolving challenges related to structural water remain critical goals for broader adoption, especially in applications such as electric vehicles where higher energy density is essential.[85]

Overall, PBAs present a compelling combination of performance, cost-effectiveness, and manufacturing simplicity, positioning them as strong candidates within the SIB landscape. Continued advances in defect minimisation, water-free synthesis, and mixed-metal chemistries are poised to further strengthen the commercial prospects of PBAs for next-generation energy storage technologies.

3 Negative electrode materials

3.1. Overview of anode materials for SIBs

The selection of a suitable anode materials remains a central challenge in the design of SIBs. Graphite does not accommodate sodium effectively under standard conditions because of the energetics associated with surface interactions and intercalation of sodium compared to lithium.[88,89] As a result, alternative materials and strategies have been developed to address the electrochemical and structural requirements specific to sodium.[88,89]

Metallic sodium offers the highest theoretical capacity and the lowest redox potential among known candidates.[90] However, dendritic growth, unstable SEI formation, and low coulombic efficiency have so far precluded its widespread adoption.[90] Recent advances in interfacial engineering and 3D host design have enabled progress, but practical implementation remains limited.[90]

Current anode materials for SIBs are generally classified into four categories which include (i) insertion type, (ii) conversion type, (iii) alloy type, and (iv) conversion-alloy type compounds. Each class offers distinct trade-offs between capacity, reversibility, rate performance, and structural stability.[89] Some materials also exhibit multiple reaction types depending on potential.

3.1.1. Intercalation-type anodes. Intercalation-type materials can be broadly classified into (a) carbon-based and (b) titanium-based oxides. Their stable lattice frameworks allow reversible insertion and extraction of sodium-ion with minimal structural distortion, yielding excellent cycling stability. Hard carbon is an established anode for SIB,[91] nonetheless other carbon-based anodes have been investigated to develop an alternative. Among carbon-based materials, graphite was the earliest candidate due to its abundance, low cost, and environmental benignity.[92] However, graphite fails to reversibly intercalate Na^+ ions under standard conditions because of the weak van der Waals interactions between the sodium-ion and graphene layers.[93]

Recent advancements have demonstrated successful Na intercalation in graphite through co-solvation with ether-based electrolytes, though at relatively high redox potentials (0.6–0.8 V *vs.* Na/Na^+), limiting overall energy density.[92] Lower-dimensional carbon materials, including carbon nanotubes (CNTs) and reduced graphene oxide (rGO), have also been investigated. By tailoring morphology, particle size, and defect density, CNTs can enhance sodium-ion storage and rate capability. Likewise, heteroatom-doped rGO exhibits superior sodium-ion adsorption and improved capacity compared to pristine graphene (Fig. 9a).

Hard carbon is currently the most widely adopted anode material for SIBs. It is produced through the pyrolysis of organic precursors, yielding a disordered structure composed of loosely

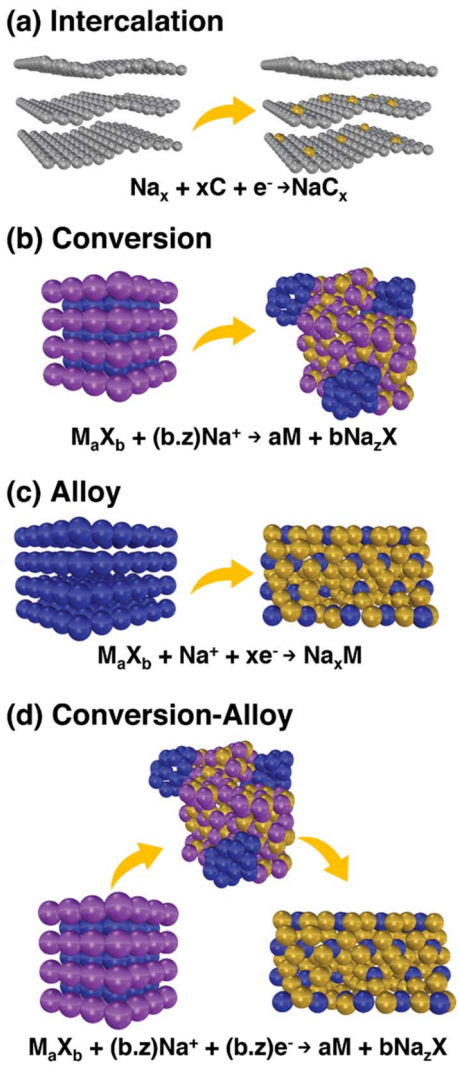

Fig. 9 Schematic representation of sodiation–desodiation mechanisms in sodium-based anode materials. M represents transition metals or Group IV, V elements and X denote anions such as O, S, Se, Te, *etc*. The mechanisms illustrated are (a) intercalation, (b) conversion, (c) alloy, and (d) conversion-alloy.

stacked graphene layers and nanoscale pores.[94] Unlike graphite, which lacks the structural "openness" required for sodium insertion, hard carbon accommodates sodium through multiple storage mechanisms distributed across its heterogeneous microstructure.[95]

Initial models proposed a two-step filling process in which sodium clusters nucleate and grow within the carbon pores.[96] Subsequent refinements have introduced alternative frameworks that include combined adsorption and intercalation processes as well as the influence of residual pore filling effects.[97] Despite these developments the detailed mechanism remains under investigation. The relative contributions of the graphitic domains and the pore structure are not yet fully resolved.

It is worth noting that the electrochemical performance of hard carbon is highly dependent to its structural features. These are influenced by the composition of the precursor material as well as the temperature and conditions of carbonisation.[98,99] Precursors derived from biomass exhibit a wide range of structural variations depending on the relative content of cellulose and lignin. High cellulose content tends to yield closed micropores while lignin-rich sources suppress graphitisation and promote porosity.[96] For example, hard carbon prepared from corn cob precursors has shown significant low-voltage plateau capacity which is attributed to the formation of sodium clusters within the micropores.

Carbonisation temperature directly affects the size and accessibility of pores. At lower temperatures sodium primarily occupies pores smaller than approximately 4 Å. As the temperature increases medium-sized pores in the range of 6 to 8 Å become available.[98] These observations underscore the importance of controlling pore size distribution to enhance both capacity and transport kinetics.

The disordered nature of hard carbon and the variety of sodium host environments contribute to its potential but also to ongoing uncertainty. Resolving the storage mechanism remains a key step toward rational design to improve cell efficiency and higher rate capability in SIB full cells.

Beyond precursor selection and temperature control, heteroatom doping has emerged as a versatile strategy to modulate the microstructure and functional properties of hard carbon. The introduction of elements such as boron, nitrogen, phosphorus, or sulfur into the carbon lattice can alter local electronic environments and adjust surface polarity. These effects influence sodium adsorption energies, charge distribution, and SEI composition. For example, nitrogen doping introduces pyridinic and graphitic nitrogen sites, which enhance conductivity and provide additional adsorption sites for sodium ions. Boron doping, in contrast, can improve sodium binding and contribute to more stable SEI formation by modifying the surface reactivity of the carbon framework.

Structural templating represents another effective method for optimising pore architecture. Hard templates, such as silica nanoparticles, can be used to generate ordered mesopores, while soft templates derived from block copolymers or surfactants promote the formation of interconnected networks. These templated materials offer improved ion transport pathways, reduced diffusion barriers, and greater electrolyte accessibility. When combined with controlled doping, templated hard carbons exhibit enhanced rate capability and improved cycling stability under high current densities. In particular, synergistic approaches that combine doping and templating have shown promise in simultaneously tuning both chemical functionality and structural hierarchy.

The electrolyte plays a critical role in governing the interfacial behaviour of hard carbon electrodes. In particular, the formation and composition of the SEI influence both sodium-ion transport kinetics and long-term cycling stability.[99,100] Unlike lithium-ion systems with relatively well-characterised SEI behaviour, SIBs show more complex and electrolyte-dependent interfacial responses.[101] Comparative studies between carbonate-based and ether-based electrolytes have revealed distinct differences in SEI morphology and

electrochemical response.[101] Ether systems tend to generate thicker SEI layers with increased organic content. While these layers may offer enhanced passivation, they also present greater resistance to ion transport which compromises rate performance. In contrast carbonate electrolytes produce thinner and more inorganic SEI structures but are often associated with poorer long-term stability.[102]

One of the main challenges for hard carbon anodes is their low ICE caused by irreversible sodium consumption during the first cycle.[103] This results from side reactions with the electrolyte and sodium trapping in structural defects and micropores, ultimately lowering the practical energy density of full cells and necessitating corrective strategies such as pre-sodiation. Recent studies highlight the role of internal pore structure in SEI evolution. Ink-bottle-shaped nanopores restrict uniform electrolyte infiltration, delaying SEI formation across the carbon matrix. Osmotic and capillary effects further contribute to spatial inhomogeneity during the early stages.[104] Allowing the assembled cell to rest prior to cycling improves electrolyte penetration and promotes more consistent interphase formation. In one case, a ten-day equilibration in an ether-based system yielded an ICE above 98% (Fig. 10a–d).

Addressing the irreversible sodium loss during early cycling is essential for realising high-efficiency SIBs. Pre-sodiation has become a central strategy for compensating sodium loss during early cycling, which otherwise limits coulombic efficiency and complicates full-cell balancing. One established approach is chemical pre-sodiation using for example sodium bis(2-methoxyethoxy) aluminium hydride which delivers sodium *in situ* while generating a stabilising Al_2O_3 layer on the surface.[105] This method improves ICE from below 70% to over 90%. Other compounds, such as sodium borohydride, release metallic sodium. Though this improves conductivity and SEI quality, the long-term structural impact remains uncertain. These materials demonstrate the potential of combining sodium replenishment with interfacial engineering to address multiple performance bottlenecks simultaneously.

Titanium-based oxides represent another important class of intercalation-type anodes, exhibiting stable redox potentials and excellent structural reversibility. TiO_2 exists in multiple polymorphs (rutile, anatase, bronze, and hollandite), each offering distinct Na^+ storage characteristics.[92,106] Layered $Na_2Ti_3O_7$, for example, operates at a low potential (~0.3 V) but suffers from poor ionic conductivity and limited capacity retention. Tunnel-type $Na_2Ti_3O_7$, in contrast, provides improved ion transport and cycling stability, albeit with relatively low storage capacity.[92]

3.1.2. Conversion-type anodes. In conversion-type anodes (Fig. 9b), sodium storage occurs through a redox-driven transformation of the host material into metallic nanoparticles and sodium compounds (*e.g.*, Na_2O). These systems deliver high theoretical capacities owing to multielectron transfer processes. However, the significant volume expansion accompanying the conversion reaction leads to active material pulverisation, electrical isolation, and rapid capacity fading.

Early studies on $NiCo_2O_4$ demonstrated an eight-electron transfer reaction forming Ni, Co, and Na_2O. Iron-based oxides, such as Fe_2O_3 and Fe_3O_4, were later explored due to their low cost and environmental friendliness, but these materials also suffered from low conductivity and substantial volume change.[107,108] Other oxides, including CuO and MnO, were similarly investigated.[109]

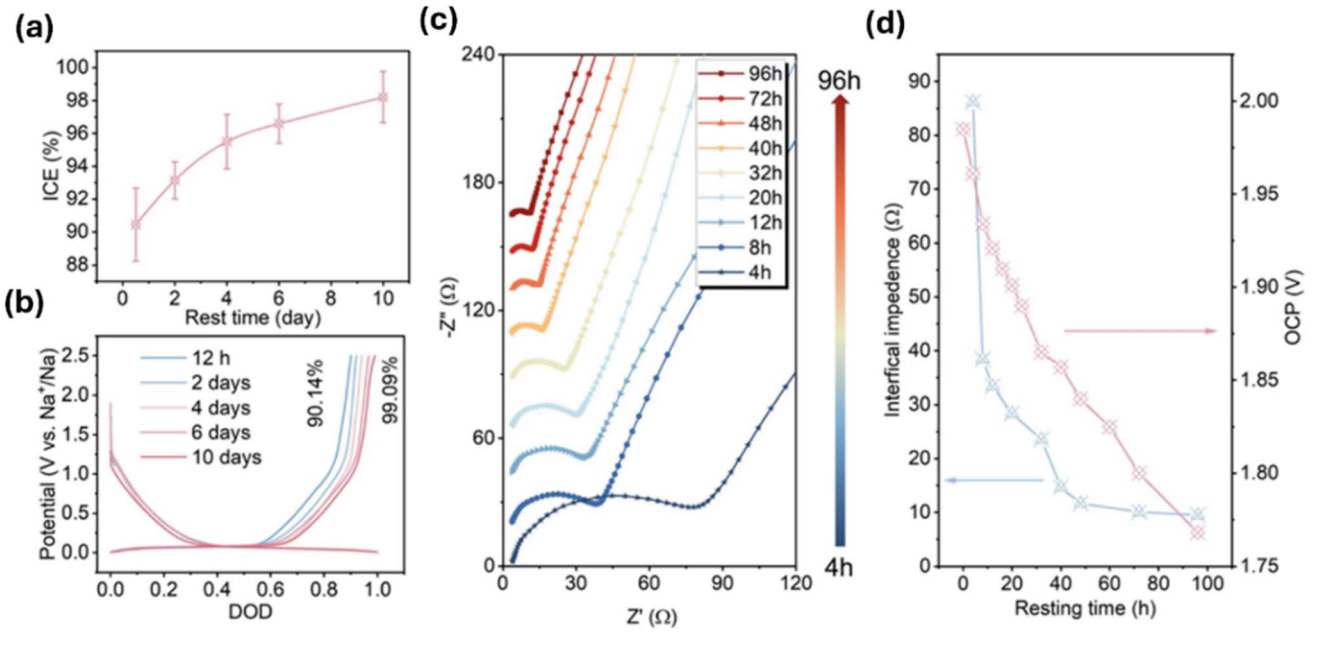

Fig. 10 (a) ICE *vs.* rest time. (b) Charge–discharge of hard carbon after different rest times. (c) Nyquist plot of hard carbon at different rest times. (d) Interfacial resistance and open circuit potential *versus* rest time. Reproduced from ref. 104 with permission from Springer Nature, copyright 2024.

Transition metal chalcogenides (*e.g.*, sulfides and selenides) emerged as attractive alternatives due to the relatively weaker Na–S and Na–Se bonds, which enhance reversibility. Iron sulfides, molybdenum sulfides, and iron selenides with nanoscale architectures have been developed to accommodate large volume changes and minimise mechanical stress. Transition metal nitrides have also been explored as promising candidates owing to their metallic conductivity and chemical stability.

Conversion-type anodes operate through reversible bond-breaking and bond-forming reactions between the active material and sodium ions. During these electrochemical reactions, the TM is reduced upon sodium insertion, leading to multiple phase transitions during the charge/discharge process.[110] These transitions involve multielectron transfer associated with the reduction and oxidation of the transition metal, thereby enabling high theoretical capacities. The overall conversion reaction in SIBs can be expressed as:

$$M_aX_b + (b \times z)Na \leftrightarrow aM + bNa_zX$$

Here, M represents a transition metal (such as Fe, Co, Ni, *etc.*), and X denotes a nonmetal element (O, F, S, Se, *etc.*). In addition to transition metals, several semimetals (Si, Ge, Sn, Sb, Bi) can undergo reduction and subsequently form alloys with sodium *via* a conversion-alloy mechanism.[111]

During sodiation, the TM phase separates as metallic nanoparticles while Na_x forms a surrounding matrix, generating a conductive network that facilitates charge transfer. Despite their high theoretical capacities, conversion-type anodes face critical limitations in practical applications, primarily due to severe volume changes that lead to structural pulverisation and poor cycling stability. Moreover, these materials often exhibit large voltage hysteresis (typically exceeding 0.5 V) due to compositional inhomogeneity during cycling. The low ICE, stemming from incomplete reconversion and electrolyte decomposition, further restricts their commercial viability compared to intercalation-based anodes.[110]

To address these challenges, extensive research efforts have focused on structural and compositional engineering. Strategies such as nanostructure design, nanocomposite formation, defect engineering, and electrolyte optimisation have shown promising improvements.[110] For instance, a Bi_2S_3–VS_4 composite anchored on reduced graphene oxide, synthesised *via* a facile one-pot method, exhibited enhanced rate capability and prolonged cycling life of up to 200 cycles.[112] Similarly, a carbon-modified $SbSe_3$–WSe_2 heterostructured nanofiber demonstrated a capacity of 553.7 mAh g^{-1} after 250 cycles at a high current density of 2 Ag^{-1}. The carbon network facilitated superior electron transport and provided abundant active sites for sodium-ion storage. Moreover, the intrinsic electric field at the Sb–W–Se heterointerface promoted sodium-ion diffusion, thus improving both conversion and alloying processes.[113]

Another example involves a metal–organic framework (MOF) derived core–shell petal-type anode prepared through the selenisation and carbonisation of $MoWSe_2$–WO_3–C.[114] This anode exhibited a reversible capacity of 384.3 mAh g^{-1} even after 950 cycles at 10 Ag^{-1}. The cycling stability was attributed to the mechanically robust 3D petal-like core–shell structure, which provided structural integrity, uniform carbon distribution for enhanced electronic conductivity, and an efficient $MoWSe_2$–WO_3–C heterostructure facilitating sodium-ion transport.[114]

3.1.3. Alloy-type anodes. Alloy-type anode materials exhibit theoretical capacities one to three times higher than those of conversion-type counterparts. Typically composed of group IVA and VA elements (*e.g.*, Si, Ge, Sn, Sb, Bi), these materials undergo reversible alloying/dealloying reactions with Na^+ (Fig. 9c).[115] However, their practical application is hampered by severe volume expansion caused by the insertion of large-radius sodium-ions.[116] This expansion induces mechanical degradation, particle pulverisation, and loss of electrical contact, leading to poor cycling stability and low rate performance. Additionally, large initial irreversible capacity and sluggish kinetics further limit their feasibility in commercial SIB systems.

Stabilisation of alloy-type anodes through electrolyte engineering has been systematically investigated. A low electrolyte concentration 0.1 M $NaBPh_4$ in 1,2-dimethoxyethane was employed for Sn and Bi alloy anodes.[117] Sodium tetraphenylborate was selected due to its weakly coordinating anion, which effectively mitigates anode corrosion.[117] At such low salt concentrations, strong solvent–cation interactions dominate, distancing anions from the alloy surface and thereby suppressing parasitic side reactions.

Liquid alloy systems, such as Na–K alloys, have recently attracted interest due to their fluidity, which imparts self-healing characteristics and suppresses dendrite formation.[118] These alloys are typically infused into porous current collectors under high pressure and temperature. However, their practical deployment is limited by electrolyte leakage arising from the absence of a mechanically robust and chemically stable SEI. To address this limitation, semi-solid Na-alloy systems have been developed; nevertheless, leakage issues persist due to the strong affinity between Na metal and the Na–K liquid phase.[118]

To mitigate mechanical degradation during the 420% volume change associated with the Sn–Na alloying/dealloying process, Jian *et al.*[119] engineered nitrogen-doped carbon-coated tin nanorods. The surface-modified nanostructure enhanced electronic and sodium-ion transport properties, suppressed pulverisation, and enabled exceptional cycling stability, maintaining performance for up to 10 000 cycles. When paired with a $Na_3V_2(PO_4)_3$ (NVP) cathode in a full-cell configuration, the N-doped carbon/tin nanorod anode delivered an impressive energy density of 215 Wh kg^{-1}.[119]

3.1.4. Conversion-alloy type anodes. Materials such as oxides, sulfides, and selenides of group IVA and VA elements exhibit a hybrid conversion-alloying mechanism.[120] During sodiation, these materials initially undergo a conversion reaction forming Na_2X and metallic M, followed by alloying of M with sodium-ions (Fig. 9d)[92] The conversion products act as a structural buffer, mitigating volume variation during alloying. Consequently, these anodes combine the advantages of both mechanisms, offering high capacities and relatively low operating voltages.

Tin and antimony oxides possess theoretical specific capacities exceeding 1000 mAh g^{-1}, yet their practical performance is severely compromised by irreversible electrochemical reactions and sluggish reaction kinetics, resulting in substantially lower delivered capacities.[121] To mitigate these limitations, surface modification with functionalised carbon has proven effective in enhancing electrochemical performance.[121]

Furthermore, the construction of heterostructures has emerged as a powerful strategy to improve the sodium-storage properties of these materials. For instance, a heterostructure $Sb_2S_3/SnS_2/C$ composite demonstrated good cycling stability, retaining a reversible capacity of 642 mAh g^{-1} after 600 cycles.[122] Similarly, a Bi_2Se_3/Bi_2O_3 heterostructure delivered a stable capacity of 310 mAh g^{-1} over 100 cycles, benefiting from the synergistic interplay between the Bi_2Se_3 and Bi_2O_3 nanostructures.[123]

However, the performance of conversion-alloy anodes remains constrained by drastic volume fluctuations and low electronic conductivity, which deteriorate cycling stability and rate capability. To overcome these issues, research has focused on structural optimisation, nanocomposite engineering, and electrolyte modification to enhance sodium-ion transport, electrical conductivity, and mechanical robustness.[92]

3.2. Anode free sodium batteries

In contrast to conventional intercalation or alloying-based anodes, the anode-free sodium-ion battery (AFSIB) architecture relies on the direct electrochemical deposition of sodium ions onto the surface of a current collector.[124] This design significantly enhances the energy density by eliminating the need for a pre-formed anode, thereby reducing both material costs and fabrication complexity. Furthermore, the absence of an anode material decreases the overall weight and volume of the cell, offering an additional improvement in gravimetric and volumetric energy density.[124]

During charging, sodium ions migrate from the cathode and are electroplated onto the current collector, temporarily forming a metallic sodium layer that functions as an *in situ* anode. Upon discharging, the deposited sodium is stripped from the collector and reinserted into the cathode host structure. However, unlike conventional sodium-ion cells, the anode-free configuration possesses a limited sodium reservoir. Consequently, any irreversible loss of active sodium-arising from side reactions or incomplete stripping, leads to rapid capacity fading and poor cycling stability.

Despite these advantages, AFSMBs face several formidable challenges. The spontaneous reaction between freshly deposited sodium and the electrolyte during SEI formation consumes active sodium, resulting in low ICE.[124] Moreover, the heterogeneous nucleation of sodium on the current collector often induces dendritic growth, which can lead to internal short-circuiting. Additionally, mechanical stress generated by repeated sodium plating and stripping causes interfacial degradation, thereby destabilising the electrode/electrolyte interface and deteriorating long-term cycling performance.[124]

To mitigate these issues, researchers have explored advanced current collector designs. For instance, a three-dimensional (3D) conductive carbon microporous fibre framework doped with nitrogen and phosphorus was investigated as a current collector for anode-free architectures.[125] This 3D scaffold effectively reduced local current density and regulated sodium-ion flux distribution. The large surface area also accommodated the volumetric changes associated with Na deposition and stripping, leading to improved cycling stability. As a result, a coulombic efficiency of 99.97% at 10 mA cm^{-2} with over 2000 stable cycles was achieved. Furthermore, when paired with a $Na_3V_2(PO_4)_3$ (NVP) cathode, a foldable pouch cell was successfully fabricated, demonstrating excellent flexibility and mechanical robustness.[125]

Functionalisation of metallic current collectors has also been explored. A porous aluminium current collector was fabricated through the electrodeposition of zinc on an aluminium foil, followed by the evaporation of zinc to create uniform pores.[126] The resulting porous Al framework acted as a sodiophilic host, enhancing interfacial reaction kinetics and suppressing dendrite formation by homogenising current distribution. AFSMBs utilising this Al foam exhibited nearly perfect coulombic efficiency, even at high areal capacities of 20 mAh cm^{-2}. Additionally, an anode-free pouch cell employing a $Na_3V_2(PO_4)_2F_3$ cathode delivered a discharge capacity of 99.9 mAh g^{-1} with a coulombic efficiency of 93.6%.[126]

To further address interfacial instability, various solid-state electrolyte systems have been investigated. Incorporating solid electrolytes in AFSMBs improves mechanical integrity by maintaining stack pressure, enhancing interfacial contact, and minimising side reactions that consume active sodium. For example, when sodium borohydride ($NaBH_4$) was used as a solid electrolyte, an ICE of 64% was achieved.[127] In contrast, cells employing Na_3PS_4 exhibited a significantly lower ICE (4%), attributed to the reductive decomposition of Na_3PS_4 to Na_3P at low potentials. These findings highlight that the electrochemical stability of the solid electrolyte with sodium metal is a crucial parameter in the design of all-solid-state anode-free batteries.[127]

Sodium deposition occurs at the interface where sodium-ions and electrons meet on the current collector surface. Limited contact between these charge carriers restricts the active deposition area, leading to uneven plating/stripping. Replacing conventional Al foil with pelletised aluminium powder improved uniform contact with the solid electrolyte, thereby enhancing sodium-ion plating/stripping behavior.[127] This modification increased the ICE from 64% (for planar Al foil) to 93% for the pelletised Al powder collector.[127]

In the case of anode-free seawater batteries, a novel poly(-ethylene oxide) (PEO)-based ionic liquid solid electrolyte with an ionic conductivity of 1 mS cm^{-1} was developed.[128] This flexible electrolyte comprises PEO, NaFSI salt, and 1-butyl-1-methylpyrrolidinium bis(fluorosulfonyl)imide ionic liquid, forming a free-standing polymer matrix that combines high ionic conductivity with mechanical stability, an attractive feature for flexible and sustainable sodium-based energy storage systems.[128]

4. Commercial viability of SIBs

The structural and electrochemical parallels between LIBs and SIBs have laid the foundation for the rapid development of SIB technology. While the two systems share similar working principles, the larger ionic radius of sodium-ion (1.02 Å) compared to lithium-ion (0.76 Å) presents unique challenges in the sodium system, particularly in terms of sluggish diffusion kinetics, phase instability, and compatibility with electrode materials.[129] Despite these hurdles, the commercial interest in SIBs is intensifying due to a convergence of factors, including material abundance, cost-effectiveness, and improved safety characteristics.

One notable advantage of SIBs lies in their safer design configuration. In LIBs, the use of a copper current collector at the anode poses a challenge for transportation at 0 V, as copper can dissolve at low potentials, increasing the risk of internal short circuits. Additionally, aluminium is unsuitable for the anode current collector in LIBs due to its tendency to alloy with lithium. In contrast, sodium does not alloy with aluminium under standard operating conditions,[130] enabling the use of aluminium current collectors for both electrodes in SIBs. This not only enhances safety during shipping, logistics and storage but also reduces the overall material cost, making SIBs more attractive for large-scale deployment.

SIBs are particularly well-suited for grid-scale storage, where cost, safety, and sustainability are prioritised over energy density. The natural abundance of sodium and the potential for low-cost cathode chemistries, especially iron and manganese-based layered oxides, polyanionics and PBAs make SIBs a strong candidate for stationary storage and low-cost mobility solutions. In contrast, electrode chemistries rich in nickel, cobalt, or vanadium, while offering higher capacities, suffer from limited resource availability and higher cost, thereby restricting their scalability especially when competing with $LiFePO_4$ containing lithium-ion batteries.

Despite significant progress, transitioning SIBs from laboratory innovation to industrial deployment remains a major challenge. Since 2020, over 1500 research publications have focused on sodium-based cathode materials, reflecting the growing academic interest in this field. However, this momentum has not yet fully translated into standardised practices or commercial scaling.

A crucial step in bridging this gap is the development of standardised electrochemical testing protocols. Current evaluations predominantly rely on coin cells with low areal capacities, which may not accurately represent practical battery performance. Moving toward multilayer pouch cells with areal capacities exceeding 4 mAh cm^{-2} is essential for evaluating real-world viability. Furthermore, the widespread use of sodium metal as the counter electrode in half-cell configurations introduces challenges such as impedance buildup and rapid capacity fade, which are not representative of commercial full-cell conditions.[129] Thus, alternative full-cell configurations using practical electrodes are needed for reliable performance assessment.

In addition, safety remains a critical yet often underreported aspect in academic studies. Quantitative assessments of thermal behaviour, especially under high-rate or abusive conditions, must be systematically incorporated into laboratory evaluations. Establishing protocols that account for thermal runaway, internal shorting, and gas evolution will be vital for the safe integration of SIBs in real-world applications. Furthermore, and arguably the most challenging is predicting and understanding lifetime in SIBs. For example, being a large cation, sodium-ion relative to lithium-ion, the structural impact during each cycle is intuitively larger and therefore understanding the rate of capacity fade, as a function of applied current or temperature or external conditions is essential for laying the foundations of lifetime predictions.

A wave of industrial innovation is rapidly transforming SIB technology from a laboratory concept into a commercially viable reality. This progress is not confined to isolated breakthroughs but is unfolding across a diverse landscape of companies, each contributing uniquely to the evolution of SIBs. One of the earliest pioneers in this space, Faradion (UK), has emphasised safety and cost-effectiveness by leveraging layered oxide cathodes alongside aluminium current collectors on both electrodes, a design that allows for safe battery transport at 0 V, a feature not possible with traditional lithium-ion configurations.[131] This strategy aligns well with SIBs' broader promise of enhanced safety and simplified manufacturing logistics.[132]

Simultaneously, companies such as Novasis Energies (USA), in collaboration with Sharp Labs, have focused on electrochemical durability.[10] By adopting PBAs as the cathode material, their cells have achieved over 80% capacity retention after 500 cycles an encouraging benchmark for long-term stability and commercial reliability.

Further east, HiNa Battery (China) is scaling this momentum by establishing the world's first GWh-scale SIB production line.[129] Their use of Cu–Fe–Mn layered oxide cathodes already tested in electric vehicles signals a growing confidence in SIB's readiness for real-world deployment in both grid and mobility sectors. Europe is also contributing to this global effort. TIAMAT (France) is developing cylindrical cells based on the polyanionic compound $Na_3V_2(PO_4)_3F$, tailored specifically for transportation applications.[129] These chemistries offer fast kinetics and structural stability, highlighting the potential of polyanionic frameworks in next-generation SIBs.

In parallel, Natron Energy (USA) has adopted an unconventional yet promising approach, utilising PBAs for both cathode and anode in an aqueous electrolyte system. This design supports very fast 10 C charging while delivering high safety and power density features particularly attractive for applications demanding rapid charge–discharge cycles.[130] The innovation landscape also extends to Sweden, where Altris AB is tackling the challenge of scalability. By focusing on nonflammable electrolytes and low-temperature, low-pressure synthesis of PBA materials, they aim to lower the barriers to mass manufacturing without compromising safety or performance.

At the forefront of commercialisation, CATL (China), a global leader in LIBs, is applying its extensive expertise to sodium systems. Their first-generation PBA based SIB delivers an energy

density of 160 Wh kg^{-1}, with second-generation designs targeting 200 Wh kg^{-1}, approaching parity with lithium iron phosphate based LIBs.[129] This progress signals a strategic shift in the industry's outlook, where sodium-ion systems are no longer seen as niche but as serious contenders in the broader battery ecosystem. Numerous other companies and entities, predominantly in Asia have begun developing production lines for sodium-based commercial cells, some of which are commercially available at the time of the production of this article.

To further evaluate the commercial readiness of SIBs, commercially available cells from HAKADI were examined and benchmarked against conventional LIBs.[133–135] Two formats were analysed: 18 650 (1.5 Ah) and 26 700 (3.5 Ah) cylindrical cells. These cells demonstrated electrochemical performance on par with $LiFePO_4$-based LIBs, with a specific energy of approximately 120 Wh kg^{-1}. Post-mortem analyses identified hard carbon as the anode and a Na–Ni–Fe–Mn layered oxide as the cathode. Importantly, thermal characterisation (T_{max}) under varying C-rates revealed that the T_{max}/C-rate ratio was comparable to LIBs, indicating favourable thermal stability. These results underscore the promising advancements in SIB technology toward commercial viability in terms of both performance and safety.

In summary, SIBs have emerged as a compelling alternative to lithium-ion systems, particularly for stationary storage and cost-sensitive mobility applications. Continued efforts in materials research, standardisation of testing methodologies, and real-world validation are pivotal to accelerate their path toward commercialisation.

Conflicts of interest

There are no conflicts to declare.

Data availability

No primary research results, software or code have been included and no new data were generated or analysed as part of this review.

Acknowledgements

D. J. K. acknowledges support from Nano & Material Technology Development Program through the National Research Foundation of Korea (NRF) grant funded by the Korea government (MSIT) (No. RS-2025-25441820). The authors thank Dae Kyung Kim for the valuable assistance in creating the illustrations for the figures.

References

1 A. Yao, S. M. Benson and W. C. Chueh, *Nat. Energy*, 2025, **10**, 404–416.
2 A. Namazbay, M. Karlykan, L. Rakhymbay, Z. Bakenov, N. Voronina, S.-T. Myung and A. Konarov, *Energy Storage Mater.*, 2025, **77**, 104212.
3 S. Kim, D. Seo, X. Ma, G. Ceder and K. Kang, *Adv. Energy Mater.*, 2012, **2**, 710–721.
4 R. Qiu, D. Ma, H. Zheng, M. Liu, J. Cai, W. Yan and J. Zhang, *Nano Energy*, 2024, **128**, 109920.
5 Y. Miao, P. Yu, F. Yang, Y. Zhao, H. Xu and J. Wang, *ACS Appl. Mater. Interfaces*, 2025, **17**, 1064–1076.
6 H. Zhang, L. Wang and P. Zuo, *J. Mater. Chem. A*, 2024, **12**, 30971–31003.
7 Z. Zhang, R. Wang, J. Zeng, K. Shi, C. Zhu and X. Yan, *Adv. Funct. Mater.*, 2021, **31**, 2106047.
8 C. Che, F. Wu, Y. Li, Y. Li, S. Li, C. Wu and Y. Bai, *Adv. Mater.*, 2024, **36**, 2402291.
9 Y. Wu, M. Liu, A. Zhang, L. Ma and L. Ouyang, *Mater. Today*, 2025, **88**, 1028–1042.
10 J.-M. Tarascon, *Joule*, 2020, **4**, 1616–1620.
11 Y. Liu, Q. Shen, X. Zhao, J. Zhang, X. Liu, T. Wang, N. Zhang, L. Jiao, J. Chen and L. Fan, *Adv. Funct. Mater.*, 2020, **30**, 1907837.
12 C. Wang, L. Liu, S. Zhao, Y. Liu, Y. Yang, H. Yu, S. Lee, G.-H. Lee, Y.-M. Kang, R. Liu, F. Li and J. Chen, *Nat. Commun.*, 2021, **12**, 2256.
13 L. Yang, L. Kuo, J. M. López del Amo, P. K. Nayak, K. A. Mazzio, S. Maletti, D. Mikhailova, L. Giebeler, P. Kaghazchi, T. Rojo and P. Adelhelm, *Adv. Funct. Mater.*, 2021, **31**, 2102939.
14 Y. Shi, P. Jiang, S. Wang, W. Chen, B. Wei, X. Lu, G. Qian, W. H. Kan, H. Chen, W. Yin, Y. Sun and X. Lu, *Nat. Commun.*, 2022, **13**, 7888.
15 E. Gabriel, Z. Wang, V. V. Singh, K. Graff, J. Liu, C. Koroni, D. Hou, D. Schwartz, C. Li, J. Liu, X. Guo, N. C. Osti, S. P. Ong and H. Xiong, *J. Am. Chem. Soc.*, 2024, **146**, 15108–15118.
16 W. Zuo, J. Qiu, X. Liu, F. Ren, H. Liu, H. He, C. Luo, J. Li, G. F. Ortiz, H. Duan, J. Liu, M. S. Wang, Y. Li, R. Fu and Y. Yang, *Nat. Commun.*, 2020, **11**, 3544.
17 Y. Wang, Z. Feng, P. Cui, W. Zhu, Y. Gong, M.-A. Girard, G. Lajoie, J. Trottier, Q. Zhang, L. Gu, Y. Wang, W. Zuo, Y. Yang, J. B. Goodenough and K. Zaghib, *Nat. Commun.*, 2021, **12**, 13.
18 J. Jin, Y. Liu, X. Zhao, H. Liu, S. Deng, Q. Shen, Y. Hou, H. Qi, X. Xing, L. Jiao and J. Chen, *Angew. Chem.*, 2023, **135**, e202219230.
19 Z. Wu, Y. Ni, S. Tan, E. Hu, L. He, J. Liu, M. Hou, P. Jiao, K. Zhang, F. Cheng and J. Chen, *J. Am. Chem. Soc.*, 2023, **145**, 9596–9606.
20 L. Sun, Y. Xie, X. Liao, H. Wang, G. Tan, Z. Chen, Y. Ren, J. Gim, W. Tang, Y. He, K. Amine and Z. Ma, *Small*, 2018, **14**, 1704523.
21 X. G. Yuan, Y. J. Guo, L. Gan, X. A. Yang, W. H. He, X. S. Zhang, Y. X. Yin, S. Xin, H. R. Yao, Z. Huang and Y. G. Guo, *Adv. Funct. Mater.*, 2022, **32**, 2111466.
22 Y. Yu, D. Ning, Q. Li, A. Franz, L. Zheng, N. Zhang, G. Ren, G. Schumacher and X. Liu, *Energy Storage Mater.*, 2021, **38**, 130–140.
23 Y. Xiao, H. Wang, H. Hu, Y. Zhu, S. Li, J. Li, X. Wu and S. Chou, *Adv. Mater.*, 2022, **34**, 2202695.

24 T. Zhang, M. Ren, Y. Huang, F. Li, W. Hua, S. Indris and F. Li, *Angew. Chem., Int. Ed.*, 2024, **63**, e202316949.
25 T. Cui, L. Liu, Y. Xiang, C. Sheng, X. Li and Y. Fu, *J. Am. Chem. Soc.*, 2024, **146**, 13924–13933.
26 Y. Dang, Z. Xu, Y. Wu, R. Zheng, Z. Wang, X. Lin, Y. Liu, Z.-Y. Li, K. Sun, D. Chen and D. Wang, *J. Energy Chem.*, 2024, **95**, 577–587.
27 S. Feng, C. Zheng, Z. Song, X. Wu, M. Wu, F. Xu and Z. Wen, *Chem. Eng. J.*, 2023, **475**, 146090.
28 L. Li, T. Liu, M. Ding, H. Yu, Z. Dou, L. Wang, X. Wu, J. Zhou and P. Zhou, *Adv. Funct. Mater.*, 2025, e14832.
29 P. Zhou, Z. Che, J. Liu, J. Zhou, X. Wu, J. Weng, J. Zhao, H. Cao, J. Zhou and F. Cheng, *Energy Storage Mater.*, 2023, **57**, 618–627.
30 L. Gao, J.-N. Yang, Q. Zheng, Y. Zhang, X. Jiang, S.-Q. Li, J.-S. Chen and K.-X. Wang, *Chem. Eng. J.*, 2025, **510**, 161580.
31 P. A. Maughan, A. B. Naden, J. T. S. Irvine and A. R. Armstrong, *Commun. Mater.*, 2023, **4**, 6.
32 S. Sun, X. Zhu, H. Dong, Y. Feng, Y. Tang, M. Li, S. Xu, H. Xin, C. Ma, G. Wei, L. Hu, H. Qin, M. Liu, Y. Xiao, B. Xiao and P. Wang, *Adv. Funct. Mater.*, 2025, **35**(41), 2503900.
33 S. Li, W. Zhou, F. Liu, C. Guan, X. Gao, Y. Zhang, R. Jin, Y. Lai and Z. Zhang, *Adv. Energy Mater.*, 2025, **15**, 2403955.
34 C. Zhao, F. Ding, Y. Lu, L. Chen and Y. Hu, *Angew. Chem., Int. Ed.*, 2020, **59**, 264–269.
35 H. Wang, Y. Mei, J. Gao, L. Ni, N. Hong, L. Ma, G. Kwon, J. Huang, Y. He, W. Deng, G. Zou, H. Hou, C. Liang, T. Liu, X. Ji and K. Amine, *J. Am. Chem. Soc.*, 2025, **147**, 4810–4820.
36 H. Wang, X. Gao, S. Zhang, Y. Mei, L. Ni, J. Gao, H. Liu, N. Hong, B. Zhang, F. Zhu, W. Deng, G. Zou, H. Hou, X.-Y. Cao, H. Chen and X. Ji, *ACS Nano*, 2023, **17**, 12530–12543.
37 M. Li, C. Sun, Q. Ni, Z. Sun, Y. Liu, Y. Li, L. Li, H. Jin and Y. Zhao, *Adv. Energy Mater.*, 2023, **13**, 2203971.
38 H. Dai, Y. Xu, Y. Wang, F. Cheng, Q. Wang, C. Fang, J. Han and P. K. Chu, *ACS Appl. Mater. Interfaces*, 2024, **16**, 7070–7079.
39 Q. Xiao, Y. Li, K. Wang, C. Ma, B. Liu and Y. Zhao, *J. Mater. Chem. A*, 2025, **13**, 3727–3734.
40 R. Guan, X. Zeng, X. Zhou, Y. Hu, C. Wen, D. Zhang, L. Zeng and Y. Gong, *Sustain. Energy Fuels*, 2025, **9**, 4172–4180.
41 X. Zhang, X. Yin, J. Xie, M. Wang, H. Ma, M. Tang and Y. Cao, *J. Power Sources*, 2025, **635**, 236531.
42 P. Chu, H. Fan, F. Ji, Y. Shao, Y. Chen, L. Lu, N. Wu, A. Zhao, X. Li and Y. Cao, *ACS Appl. Energy Mater.*, 2025, **8**, 9222–9229.
43 J. Xiao, J. Si, B. Pan and C. Chen, *Small*, 2025, **21**, 2412671.
44 T. Zhang, Y. Li, Z. Song, Y. Huang, F. Li, S. Cheng and F. Li, *J. Energy Chem.*, 2025, **103**, 294–315.
45 Y. Li, G. Liu, J. Che, L. Chen, X. Wang, G. Wang, L. Lei, J. Hou, S. Li, J. Wang, Y. Xu and Y. Zhao, *Interdiscip. Mater.*, 2025, **4**, 24–51.
46 Y. Zhang, G.-Q. Liu, Q. Sun, D. Qiao, J. Chen, L. Wen and M. Zhao, *J. Energy Storage*, 2024, **102**, 114212.
47 C. Zhao, Z. Yao, Q. Wang, H. Li, J. Wang, M. Liu, S. Ganapathy, Y. Lu, J. Cabana, B. Li, X. Bai, A. Aspuru-Guzik, M. Wagemaker, L. Chen and Y.-S. Hu, *J. Am. Chem. Soc.*, 2020, **142**, 5742–5750.
48 C. Gauckler, M. Dillenz, F. Maroni, L. F. Pfeiffer, J. Biskupek, M. Sotoudeh, Q. Fu, U. Kaiser, S. Dsoke, H. Euchner, P. Axmann, M. Wohlfahrt-Mehrens, A. Groß and M. Marinaro, *ACS Appl. Energy Mater.*, 2022, **5**, 13735–13750.
49 L. Xie, W. Lu, L. Li, M. Li, X. Wang and Z. Luo, *ChemistrySelect*, 2024, **9**, e202304590.
50 Q. Shi, R. Qi, X. Feng, J. Wang, Y. Li, Z. Yao, X. Wang, Q. Li, X. Lu, J. Zhang and Y. Zhao, *Nat. Commun.*, 2022, **13**, 3205.
51 W. Zuo, J. Qiu, X. Liu, F. Ren, H. Liu, H. He, C. Luo, J. Li, G. F. Ortiz, H. Duan, J. Liu, M.-S. Wang, Y. Li, R. Fu and Y. Yang, *Nat. Commun.*, 2020, **11**, 3544.
52 W. Zuo, X. Liu, J. Qiu, D. Zhang, Z. Xiao, J. Xie, F. Ren, J. Wang, Y. Li, G. F. Ortiz, W. Wen, S. Wu, M.-S. Wang, R. Fu and Y. Yang, *Nat. Commun.*, 2021, **12**, 4903.
53 K. Fang, J. Yin, G. Zeng, Z. Wu, Y. Tang, D. Yu, H. Luo, Q. Liu, Q. Zhang, T. Qiu, H. Huang, Z. Ning, C. Ouyang, L. Gu, Y. Qiao and S.-G. Sun, *J. Am. Chem. Soc.*, 2024, **146**, 31860–31872.
54 T. Hwang, J.-H. Lee, S. H. Choi, R.-G. Oh, D. Kim, M. Cho, W. Cho and M.-S. Park, *ACS Appl. Mater. Interfaces*, 2019, **11**, 30894–30901.
55 S. Maletti, A. Sarapulova, A. Schökel and D. Mikhailova, *ACS Appl. Mater. Interfaces*, 2019, **11**, 33923–33930.
56 T. Yuan, P. Li, Y. Sun, H. Che, Q. Zheng, Y. Zhang, S. Huang, J. Qiu, Y. Pang, J. Yang, Z. Ma and S. Zheng, *Adv. Funct. Mater.*, 2025, **35**, 2414627.
57 X. Yang, Y. Wang, J. Wang, J. Deng and X. Zhang, *J. Phys. Chem. Solids*, 2021, **148**, 109750.
58 L. Feng, Y. Xia, J. Guo, H. Liu, Y. Hao, Z. Tian, X. Xiao, L. Feng, C. Sun, S. Qi, K. Li, Y. Li and Y. Jiang, *Chem. Eng. J.*, 2024, **496**, 154298.
59 P. Yu, C. Fang, J. Peng and S. Dou, *Matter*, 2024, **7**, 3709–3711.
60 L. Yu, Y.-X. Chang, M. Liu, Y.-H. Feng, D. Si, X. Zhu, X.-Z. Wang, P.-F. Wang and S. Xu, *ACS Appl. Mater. Interfaces*, 2023, **15**, 23236–23245.
61 X. Li, X. Shen, J. Zhao, Y. Yang, Q. Zhang, F. Ding, M. Han, C. Xu, C. Yang, H. Liu and Y.-S. Hu, *ACS Appl. Mater. Interfaces*, 2021, **13**, 33015–33023.
62 J. Lamb, K. Jarvis and A. Manthiram, *Small*, 2022, **18**, 2106927.
63 Ş. Patat, A. Şahin, Y. Taş, F. Şanlı, Y. Yılmaz and T. Öztürk, *Int. J. Energy Res.*, 2022, **46**, 22025–22037.
64 Y. Cai, Z. Luo, K. Liao, X. Xin, M. Zhou, Y.-J. Cheng, R. Liu, X. Yan, S. Papović, K. Zheng and K. Świerczek, *J. Power Sources*, 2025, **631**, 236272.
65 X. Yuan, Y. Guo, L. Gan, X. Yang, W. He, X. Zhang, Y. Yin, S. Xin, H. Yao, Z. Huang and Y. Guo, *Adv. Funct. Mater.*, 2022, **32**, 2111466.
66 T. Song, L. Chen, D. Gastol, B. Dong, J. F. Marco, F. Berry, P. Slater, D. Reed and E. Kendrick, *Chem. Mater.*, 2022, **34**, 4153–4165.

67 W. Xu, J. Zhou, Y. Zhang, N. Wang, M. Liu, X. Li, W. Zhou, Y. Xie and K. Dai, *J. Electrochem. Soc.*, 2024, **171**, 120545.
68 S. Kang, S. Park, K. W. Nam and S. Yu, *ChemElectroChem*, 2025, **12**, e202400657.
69 C. Chen, W. Huang, Y. Li, M. Zhang, K. Nie, J. Wang, W. Zhao, R. Qi, C. Zuo, Z. Li, H. Yi and F. Pan, *Nano Energy*, 2021, **90**, 106504.
70 P. Zhou, Z. Che, J. Liu, J. Zhou, X. Wu, J. Weng, J. Zhao, H. Cao, J. Zhou and F. Cheng, *Energy Storage Mater.*, 2023, **57**, 618–627.
71 Z. Hao, X. Shi, W. Zhu, Z. Yang, X. Zhou, C. Wang, L. Li, W. Hua, C. Q. Ma and S. Chou, *ACS Nano*, 2024, **18**, 9354–9364.
72 H. Dai, Y. Xu, Y. Wang, F. Cheng, Q. Wang, C. Fang, J. Han and P. K. Chu, *ACS Appl. Mater. Interfaces*, 2024, **16**, 7070–7079.
73 C. Xu, J. Zhao, C. Yang and Y.-S. Hu, *ACS Cent. Sci.*, 2023, **9**, 1721–1736.
74 X. Pu, C. Rong, S. Tang, H. Wang, S. Cao, Y. Ding, Y. Cao and Z. Chen, *Chem. Commun.*, 2019, **55**, 9043–9046.
75 F. Wu, S. Wu, X. Ye, Y. Ren and P. Wei, *Chin. Chem. Lett.*, 2025, **36**, 109851.
76 H. Li, M. Xu, H. Long, J. Zheng, L. Zhang, S. Li, C. Guan, Y. Lai and Z. Zhang, *Adv. Sci.*, 2022, **9**, 2202082.
77 B. Wu, G. Hou, E. Kovalska, V. Mazanek, P. Marvan, L. Liao, L. Dekanovsky, D. Sedmidubsky, I. Marek, C. Hervoches and Z. Sofer, *Inorg. Chem.*, 2022, **61**, 4092–4101.
78 Z. Hao, X. Shi, W. Zhu, Z. Yang, X. Zhou, C. Wang, L. Li, W. Hua, C. Q. Ma and S. Chou, *ACS Nano*, 2024, **18**, 9354–9364.
79 X. Ge, H. Li, J. Li, C. Guan, X. Wang, L. He, S. Li, Y. Lai and Z. Zhang, *Small*, 2023, **19**, 2302609.
80 W. Wang, Y. Gang, Z. Hu, Z. Yan, W. Li, Y. Li, Q.-F. Gu, Z. Wang, S.-L. Chou, H.-K. Liu and S.-X. Dou, *Nat. Commun.*, 2020, **11**, 980.
81 X. Wu, C. Wu, C. Wei, L. Hu, J. Qian, Y. Cao, X. Ai, J. Wang and H. Yang, *ACS Appl. Mater. Interfaces*, 2016, **8**, 5393–5399.
82 S. Sun, X. Jiang, Z. Wang, H. Lei, Y. Zhai and P. Wang, *Dalton Trans.*, 2025, **54**, 14254–14261.
83 J. Lee, I. Choi, E. Kim, J. Park and K. W. Nam, *iScience*, 2024, **27**, 110211.
84 S. Büchele, V. Mereacre, N. Bohn, P. Stüble, X. Wu, N. Keim, R. Xu, H. Geßwein, W. Sun, G. Vrhovac, M. Pordzik, T. Bergfeldt, S. Indris, W. Bauer, H. Ehrenberg and J. R. Binder, *Batteries Supercaps*, 2025, **8**, e202500015.
85 J. Zhou, R. C. K. Reddy, A. Zhong, Y. Li, Q. Huang, X. Lin, J. Qian, C. Yang, I. Manke and R. Chen, *Adv. Mater.*, 2024, **36**, 2312471.
86 Y. Xiao, J. Xiao, H. Zhao, J. Li, G. Zhang, D. Zhang, X. Guo, H. Gao, Y. Wang, J. Chen, G. Wang and H. Liu, *Small*, 2024, **20**, 2401957.
87 X. Zhao, Z. Xing and C. Huang, *J. Mater. Chem. A*, 2023, **11**, 22835–22844.
88 A. Kumar Prajapati and A. Bhatnagar, *J. Energy Chem.*, 2023, **83**, 509–540.
89 S. Qiao, Q. Zhou, M. Ma, H. K. Liu, S. X. Dou and S. Chong, *ACS Nano*, 2023, **17**, 11220–11252.
90 T. Li, S. Gu, W. Lv and F. Kang, *Adv. Sustainable Syst.*, 2025, **9**, 2300400.
91 W. Shao, H. Shi, X. Jian, Z. S. Wu and F. Hu, *Adv. Energy Sustain. Res.*, 2022, **3**, 2200009.
92 S. Qiao, Q. Zhou, M. Ma, H. K. Liu, S. X. Dou and S. Chong, *ACS Nano*, 2023, **17**, 11220–11252.
93 X. Zhang, J. Zhou, C. Liu, X. Chen and H. Song, *J. Mater. Chem. A*, 2016, **4**, 8837–8843.
94 U. Mittal, L. Djuandhi, N. Sharma and H. L. Andersen, *JPhys Energy*, 2022, **4**, 042001.
95 M. Thompson, Q. Xia, Z. Hu and X. S. Zhao, *Mater. Adv.*, 2021, **2**, 5881–5905.
96 D. A. Stevens and J. R. Dahn, *J. Electrochem. Soc.*, 2000, **147**, 4428.
97 C. Bommier, T. W. Surta, M. Dolgos and X. Ji, *Nano Lett.*, 2015, **15**, 5888–5892.
98 X.-S. Wu, X.-L. Dong, B.-Y. Wang, J.-L. Xia and W.-C. Li, *Renewable Energy*, 2022, **189**, 630–638.
99 X. Zhang, Y. Cao, G. Li, G. Liu, X. Dong, Y. Wang, X. Jiang, X. Zhang and Y. Xia, *Small*, 2024, **20**, 2311197.
100 Z. Tang, R. Zhang, H. Wang, S. Zhou, Z. Pan, Y. Huang, D. Sun, Y. Tang, X. Ji, K. Amine and M. Shao, *Nat. Commun.*, 2023, **14**, 6024.
101 H. Darjazi, M. Falco, F. Colò, L. Balducci, G. Piana, F. Bella, G. Meligrana, F. Nobili, G. A. Elia and C. Gerbaldi, *Adv. Mater.*, 2024, **36**, 2313572.
102 A. V. Cresce, S. M. Russell, O. Borodin, J. A. Allen, M. A. Schroeder, M. Dai, J. Peng, M. P. Gobet, S. G. Greenbaum, R. E. Rogers and K. Xu, *Phys. Chem. Chem. Phys.*, 2017, **19**, 574–586.
103 C. Wu, Y. Yang, Y. Zhang, H. Xu, X. He, X. Wu and S. Chou, *Chem. Sci.*, 2024, **15**, 6244–6268.
104 Z. Lu, H. Yang and Y. Guo, *Nat. Commun.*, 2024, **15**, 3497.
105 X. Gao, Y. Sun, B. He, Y. Nuli, J. Wang and J. Yang, *ACS Energy Lett.*, 2024, **9**, 1141–1147.
106 W. Wang, Y. Liu, X. Wu, J. Wang, L. Fu, Y. Zhu, Y. Wu and X. Liu, *Adv. Mater. Technol.*, 2018, **3**, 1800004.
107 Y. Zhang, Q. Wang, K. Zhu, K. Ye, G. Wang, D. Cao and J. Yan, *Chem. Eng. J.*, 2022, **428**, 131204.
108 B. Huang, K. Tai, M. Zhang, Y. Xiao and S. J. Dillon, *Electrochim. Acta*, 2014, **118**, 143–149.
109 T. Ma, L. Gao, Y. Liu, L. Zhang and X. Yang, *Ionics*, 2021, **27**, 1995–2003.
110 L. Fang, N. Bahlawane, W. Sun, H. Pan, B. Bin Xu, M. Yan and Y. Jiang, *Small*, 2021, **17**, 2101137.
111 C. Wu, S. Dou and Y. Yu, *Small*, 2018, **14**, 1703671.
112 D. Zhang, Y. Shao, J. Wang, Z. Li, Q. Wang, H. Sun, Q. Sun and B. Wang, *Small Struct.*, 2023, **5**, 2300217.
113 J. Wang, D. Zhang, Q. Wang, Q. Sun, H. Sun, Z. Li, H. J. Woo, S. Ramesh and B. Wang, *Adv. Funct. Mater.*, 2024, **34**, 2400261.
114 J. Wang, Y. Shao, F. Yuan, H. Sun, D. Zhang, Z. Li, S. Ramesh, H. J. Woo and B. Wang, *J. Energy Chem.*, 2023, **80**, 291–301.

115 S. Qiao, Q. Zhou, M. Ma, H. K. Liu, S. X. Dou and S. Chong, *ACS Nano*, 2023, **17**, 11220–11252.
116 X. Wang, X. Zhao and L. Wang, *Batteries Supercaps*, 2025, **8**, e20240055.
117 C. Chu, L. Zhou, Y. Cheng, X. Wang, L. Chang, P. Nie, C. Wang and L. Wang, *Chem. Eng. J.*, 2024, **482**, 148915.
118 Z. Chen, L. Wang, Z. Chen, Y. Zhong, X. Wang and J. Tu, *Adv. Funct. Mater.*, 2025, **35**(46), 2502682.
119 J. Yang, X. Guo, H. Gao, T. Wang, Z. Liu, Q. Yang, H. Yao, J. Li, C. Wang and G. Wang, *Adv. Energy Mater.*, 2023, **13**, 2300351.
120 J.-Y. Hwang, S.-T. Myung and Y.-K. Sun, *Chem. Soc. Rev.*, 2017, **46**, 3529–3614.
121 Y. Sun, Y. Yang, X.-L. Shi, G. Suo, F. Xue, J. Liu, S. Lu and Z.-G. Chen, *Chem. Eng. J.*, 2022, **433**, 133675.
122 R. Jia, L. Li, G. Shen and D. Chen, *Sci. China Mater.*, 2022, **65**, 1443–1452.
123 M. Han, Z. Zhou, Y. Li, Q. Chen and M. Chen, *J. Alloys Compd.*, 2022, **892**, 162143.
124 Z. Hu, L. Liu, X. Wang, Q. Zheng, C. Han and W. Li, *Adv. Funct. Mater.*, 2024, **34**, 2313823.
125 Y. An, Z. Pei, D. Luan, X. W. (David) Lou and A. Sci, *Sci. Adv.*, 2025, **11**, eadv2007.
126 Y. An, Z. Pei, D. Luan and X. W. (David) Lou, *Sci. Adv.*, 2025, **11**, eadv2007.
127 G. Deysher, J. A. S. Oh, Y.-T. Chen, B. Sayahpour, S.-Y. Ham, D. Cheng, P. Ridley, A. Cronk, S. W.-H. Lin, K. Qian, L. H. B. Nguyen, J. Jang and Y. S. Meng, *Nat. Energy*, 2024, **9**, 1161–1172.
128 Y. Kim, M. Künzel, D. Steinle, X. Dong, G.-T. Kim, A. Varzi and S. Passerini, *Energy Environ. Sci.*, 2022, **15**, 2610–2618.
129 Z. Cui, C. Liu and A. Manthiram, *Adv. Mater.*, 2025, **37**(46), 2420463.
130 K. Sada, J. Darga and A. Manthiram, Adv Energy Mater, *Adv. Energy Mater.*, 2023, **13**, 2302321.
131 A. Rudola, A. J. R. Rennie, R. Heap, S. S. Meysami, A. Lowbridge, F. Mazzali, R. Sayers, C. J. Wright and J. Barker, *J. Mater. Chem. A*, 2021, **9**, 8279–8302.
132 J.-M. Tarascon, *Joule*, 2020, **4**, 1616–1620.
133 K. Bischof, V. Marangon, M. Kasper, A. Aracil Regalado, M. Wohlfahrt-Mehrens, M. Hölzle, D. Bresser and T. Waldmann, *J. Power Source Adv.*, 2024, **27**, 100148.
134 B. D. K. K. Thilakarathna, T. A. Ablott, T. Cataldo, P. Ramkissoon, G. Sontam and N. Sharma, *Phys. Chem. Chem. Phys.*, 2025, **27**, 25581–25592.
135 B. D. K. K. Thilakarathna, D. Brocklebank, P. K. M. Tung, V. K. Peterson and N. Sharma, *Adv. Funct. Mater.*, 2026, **36**, e10423.